# Tsunami modeling with solid Earth–ocean–atmosphere coupled normal modes

V. Rakoto, P. Lognonné, L. Rolland

Geophysical Journal International

*Geophys. J. Int.* (2017) **211,** 1119–1138
Advance Access publication 2017 August 2
GJI Seismology

doi: 10.1093/gji/ggx322

# Tsunami modeling with solid Earth–ocean–atmosphere coupled normal modes

V. Rakoto,[1] P. Lognonné[1] and L. Rolland[2]

[1] *Institut de Physique du Globe de Paris-Sorbonne Paris Cité, Université Paris Diderot, F-*75013*, France. E-mail: rakoto@ipgp.fr*
[2] *Université Côte d Azur, OCA, CNRS, IRD, Géoazur, F-*06560 *Valbonne, France*

Accepted 2017 July 29. Received 2017 July 21; in original form 2017 April 6

## SUMMARY

Tsunamis propagating along the ocean surface generate internal gravity waves which can be detected in the atmosphere and ionosphere using airglow or total electron content (TEC) measurements. Since the late 1960s, the summation of the seismic normal modes of the Earth allows to simulate the seismic ground motions measured by seismometers. We present a detailed case study of the same technique extended to the whole solid Earth–ocean–atmosphere system and show how the extended normal modes can be used to retrieve the tsunami signature not only in the ocean but also in the atmosphere and the ionosphere. On the example of the tsunami triggered by the 2012 $M_w = 7.8$ Haida Gwaii earthquake, we illustrate the coupling mechanisms under play and investigate in details the propagation properties of Lamb modes, atmospheric gravity modes and tsunami modes. The computed normal modes show a resonance between the tsunami modes and the atmospheric gravity modes at specific frequencies: 1.5, 2 and 2.5 mHz. We highlight that only the 1.5 mHz resonance of the tsunami modes can survive up to the ionospheric heights. Other remarkable features are also presented, such as the arrival of fundamental mode gravity waves prior to the (extended in the atmosphere) tsunami wave and the increased ocean/atmosphere coupling efficiency for larger ocean depths and during daytime. At last, for the purpose of validating the technique, we apply it to three real tsunami events and evaluate how well we quantitatively reconstruct the main features of the sea level anomaly measured by Deep-ocean Assessment and Reporting of Tsunamis buoys and the global positioning system (GPS)-derived TEC perturbation.

**Key words:** Ionosphere/atmosphere interactions; Theoretical seismology; Tsunami warning; Wave propagation.



## 1 INTRODUCTION

Tsunamis are long-period oceanic gravity waves propagating over large distances (Satake 2002). They are generated by submarine earthquakes, landslides, eruptions or meteorite impacts. Since the 2004 megathrust earthquake off Sumatra and subsequent giant tsunami, the efforts in tsunami monitoring, originally focused in the Pacific area, have moved toward worldwide coverage by tsunami real-time warning systems (Titov *et al.* 2005). Real-time sea level sensors include the DART (Deep-ocean Assessment and Reporting of Tsunamis) buoy system designed to accurately measure the tsunami wave amplitude to within 3 cm despite their long horizontal wavelength (up to 200 km). A dense tsunami detection and monitoring system covering all the Earth's oceans remains costly, however, as DART systems are complex to install and require frequent maintenance. Complementary systems are therefore necessary, especially should the DART buoys be temporarily down in critical areas at the time of the tsunami wave's arrival. While regional geodetic and seismic networks can provide such additional strategies for local tsunami warning systems (Melgar & Bock 2015), it has also been suggested that tsunami monitoring and warning systems could be complemented and enhanced using ionospheric signals (Peltier & Hines 1976) measured by the global positioning system (GPS; Occhipinti *et al.* 2008; Rolland *et al.* 2010; Kamogawa *et al.* 2016) and even over-the-horizon radar systems (Coïsson *et al.* 2011). Indeed, perturbations in ionospheric signals can be measured even if the tsunami has an amplitude of only a few centimetres. Tsunami warning systems, however, require not only detection of the ionospheric signal but also a measurement processing which produces the sea level height with an acceptable error and a high success rate.

In the 1970s, Hines (1972) and Peltier & Hines (1976) suggested that events originated in the Earth, such as earthquakes, tsunamis or volcanic eruptions, trigger internal gravity waves (IGWs) that produce detectable signatures in the ionosphere. Indeed, the conservation of kinetic energy and exponential decrease in atmospheric density mean that these atmospheric waves are strongly amplified.

Thus, even if the amplitude of the tsunami wave is small compared to ocean swell wave, amplitudes at ionospheric sounding heights (from 250 to 350 km) are $10^4$–$10^5$ larger than those at ground level.

Using GPS-derived total electron content (TEC) data from the dense Japanese GPS network, Artru *et al.* (2005) were the first to observe an ionospheric disturbance associated with a tsunami, triggered by the 2001 June 23 Peru earthquake measured at $M_w = 8.2$. This novel observation was rapidly followed by the detection of similar GPS signals associated with other tsunamis (Lognonné *et al.* 2006; Rolland *et al.* 2010; Galvan *et al.* 2011; Grawe & Makela 2015), and initiated modeling efforts. Using a 3-D tsunami wavefield as input to a coupling model, Occhipinti *et al.* (2006) reconstructed the TEC ionospheric signature of the 2004 Sumatra tsunami extracted from the Jason-1 and the Topex/Poseidon satellites altimetry data. Occhipinti *et al.* (2008) then highlighted the directivity effect of the tsunami's direction of propagation with respect to the geomagnetic field orientation on the ionospheric signature amplitude. This modeling approach was then applied to the Tohoku tsunami (Occhipinti *et al.* 2011) and explained the space–time pattern observed. However, as the damping associated with molecular viscosity and thermal conduction was neglected, the simulated disturbance of the neutral atmosphere was unrealistically large, with a vertical and horizontal wind of about 600 m $s^{-1}$. The attenuation of gravity waves in the upper atmosphere, included by Hickey *et al.* (2009) and Mai & Kiang (2009), must be taken into account. The theory behind the possibility of observing the imprint of a tsunami in the Earth's atmosphere airglow (emission of light by the upper atmosphere) was investigated by Hickey *et al.* (2010). Airglow fluctuations were for the first time observed by Makela *et al.* (2011) thanks to an all-sky 630 nm imager during the Tohoku-Oki tsunami and fully modeled by Coïsson (2012). Similar observations were made for the Haida Gwaii tsunami by the same observation system in Hawaii (Grawe & Makela 2015).

These early works triggered more complete wave propagation and coupling models integrating electromagnetic field perturbations in addition to viscosity and compressibility (Kherani *et al.* 2012, 2016). Other numerical approaches have been based on fully non-linear modeling of thermospheric coupling effects (Meng *et al.* 2015), modeling of wave packets (Vadas *et al.* 2015) or application of the perturbation theory of acoustic-gravity waves (Godin *et al.* 2015). All these techniques nevertheless require the tsunami height wavefield as the source to force the atmospheric waves.

This research shows that normal modes computed in the full Earth system (i.e. solid Earth, ocean and atmosphere) are an alternative approach for computing the ionospheric signals associated with tsunamis. This formalism considers all boundary conditions and therefore implicitly integrates the full coupling between the solid, oceanic and atmospheric parts of the Earth. By their very essence, tsunami normal modes in the full Earth system represent a basis for computing any 3-D Earth response to a tsunami and therefore not only displacement in the oceanic part but also displacement or strain in the solid part and wind, temperature and density in the atmospheric part. As shown by Rolland *et al.* (2011a), the normal mode approach fully accounts for linear propagation and anelastic effects, ionospheric coupling generated by the local geomagnetic field and TEC observation geometry. The latter has a critical influence on TEC signals (Rolland *et al.* 2011a).

The solid Earth–ocean–atmosphere coupled tsunami normal modes formalism was used for the first time by Coïsson *et al.* (2015) in order to model the radio occultation perturbations generated by the IGWs associated with the 2011 Tohoku tsunami. These observations were made by one of the COSMIC satellites, which recorded an occultation over the North Pacific coinciding with the tsunami wavefront location after 2.5 hr of propagation. Observations were compared with models obtained from a summation of the tsunami normal modes of the solid Earth–ocean–atmosphere system, the latter being used to model the ionospheric response associated with the atmosphere-generated neutral wind.

This paper therefore first outlines normal mode theory and computation. It then focuses on the resonances of tsunami normal modes in the atmosphere due to interaction with gravity modes. There follows a sensitivity study of tsunami normal modes with respect to ocean depth and the atmospheric structure. The normal mode summation technique is illustrated by computing simple examples at boundary conditions, especially at the ocean bottom interface, and at the ocean surface interface. The gravity and Lamb waves are then computed and used to discuss the origin of the early ionospheric waves detected in Hawaii prior to the arrival of the tsunami and reported by Makela *et al.* (2011). In order to validate our modeling method, we then apply it to the case of three tsunami events and then compare the model data with recorded signals. The conclusion discusses both the limitations and perspectives of tsunami normal modes modeling.

## 2 NORMAL MODES MODELING

Several methods have been proposed for computing the spherical normal modes of the Earth with the atmosphere (Francis 1973, 1975; Lognonné *et al.* 1998; Watada *et al.* 2006; Kobayashi 2007). In this paper, we use the normal modes modeling approach in keeping with Lognonné *et al.* (1998) and Artru *et al.* (2001), which includes viscosity in the atmosphere and attenuation in the solid Earth, and computes the associated complex normal modes and eigenfrequencies. Other assumptions included in this modeling method are a full elastic model of the solid Earth, compressibility of fluids, gravitation and mass redistribution. Parameters not explicitly included in the model are winds, non-linearity (including the non-linearity associated with temperature change in speed of sound) and non-viscous attenuation processes in the atmosphere, such as neutral ion collision or thermal conduction (Hickey *et al.* 2009). These are, however, partially integrated through an effective viscosity and local plane wave approximation for heat diffusion. See, for example Landau & Lifshitz (1958) for such *ad hoc* approximation.

This approach was successfully used to model the atmospheric perturbations generated by Rayleigh waves and compared to data recorded by ionospheric monitoring techniques such as Doppler sounding (Artru *et al.* 2004), GPS-derived TEC (Rolland *et al.* 2011b) or thermospheric neutral density perturbations recorded by the GOCE satellite (Garcia *et al.* 2013). Applying similar research to tsunamis can be seen as the next step after these previous works, with an extension to the atmosphere of the tsunami normal modes coupling with the solid Earth and integration of water compressibility (Okal 1982; Comer 1984; Watada 2013; Tsai *et al.* 2013).

Geographic and local time variations in the atmospheric structure are integrated in the atmospheric model used for the local 1-D normal mode computations, but not in an explicit 3-D computation, for example through an aspheric perturbation theory (Lognonné 1991). This approximation is motivated by the fact that ionospheric signals generated by tsunamis are known to be produced by gravity waves created by the tsunami wavefront less than 500 km away (Occhipinti *et al.* 2010), a distance for which there is little horizontal variation in

the background atmospheric structure. This last assumption might nevertheless be less accurate at sunset and sunrise.

Other lateral variations, such as ocean depth effect, are not modeled in this paper and will have to be integrated in future efforts, possibly with theories and approaches comparable to those used to compute 3-D Rayleigh normal modes (Lognonné 1991; Millot-Langet *et al.* 2003). The first consequence, when the tsunami normal mode waveform is made through normal mode summation, is the non-accurate fit of the tsunami's arrival time, as the latter reflects the history of propagation along the path between source and observation location and therefore of ocean depth variation along that path. A second consequence is to affect the waveform, through focusing/defocusing effects due to ocean depth, coastal reflection and even islands diffraction. These effects are not modeled by conventional 1-D normal modes modeling of tsunamis.

The tsunami normal modes of a spherical non-rotating elastic isotropic Earth surrounded by a realistic 1D atmosphere are computed according to Lognonné *et al.* (1998) from 0.1 to 2.6 mHz, corresponding to a maximum angular order of $\ell \approx 500$. There are two steps to the computations. First, we compute a set of normal modes using the MINOS software (Woodhouse 1974; Gilbert & Dziewonski 1975; Woodhouse & Dahlen 1978), which solves the elastodynamic equation in the Fourier domain:

$$\omega_k^2 \mathbf{u_k} = \mathbf{A}\mathbf{u_k}, \tag{1}$$

where $\omega_k$ is the eigenfrequency of $\mathbf{u}_\mathrm{k}$, the eigenfunction of index $k$ associated with the angular order $\ell$, azimuthal order $m$ and radial order $n$. As the model is spherical, normal modes are degenerated with respect to the azimuthal order $m$ and the eigenfrequency depends only on $\ell$ and $n$. $\mathbf{A}$ is the gravitoelastic operator defined by:

$$\mathbf{A}\mathbf{u_k} = -\frac{1}{\rho_0}(\nabla \cdot (\mathbf{T} - \mathbf{u_k} \cdot \nabla \mathbf{T_0}) - \nabla \cdot (\rho_0 \mathbf{u_k})\, \mathbf{g_0} - \rho_0 \nabla \Phi_{E1}), \tag{2}$$

where $\rho_0$ is the density, $\mathbf{g}_0$ the gravity, $\mathbf{T}$ the elastic tensor, $\mathbf{T}_0$ the pre-stress tensor at equilibrium and $\Phi_{E1}$ the mass redistribution potential [see Lognonné *et al.* (1998); Dahlen & Tromp (1999) for more details]. At equilibrium, the pre-stress forces are compensated by the gravity force, so that:

$$\nabla . \mathbf{T_0} + \rho_0 \mathbf{g_0} = 0. \tag{3}$$

In this first step, both the atmospheric viscosity and the solid planet attenuation are neglected in the normal mode computation (note that the MINOS software only computes the frequency perturbation generated by attenuation and its quality coefficient, $Q$, to a first order). The boundary condition is a free surface on the top of the atmosphere generally taken at a high altitude. The Earth's internal structure model is provided by the Preliminary Reference Earth Model (PREM, Dziewonski & Anderson 1981) with an oceanic thickness corresponding to that of the tsunami observation. The surrounding atmosphere extends upwards to 550 km and its structure is modeled by the NRLMSISE-00 empirical model (Picone *et al.* 2002). Atmospheric parameters such as viscosity, speed of sound and air density are computed for the time and location of observations.

Artru *et al.* (2001) have shown that the attenuation process in the upper atmosphere cannot be neglected. The second step of our tsunami normal modes computation consists in modeling the complex normal modes, integrating several sources of attenuation. These attenuation sources are not only atmospheric viscosity but also the solid attenuation of the PREM model. The computation also takes into account the dispersion effect on seismic velocities. The normal modes equation in the Fourier domain reads:

$$\omega_k^2 \mathbf{u_k} = (\mathbf{A}(\omega) + \mathbf{i}\omega\mathbf{B})\, \mathbf{u_k}, \tag{4}$$

with $\mathbf{B}$ the viscous operator for the atmosphere and $\mathbf{A}(\omega)$ including the solid Earth attenuation. Starting from the solution obtained at the first step, the new complex eigenfunctions and eigenfrequencies are computed through a variational method (Lognonné *et al.* 1998; Artru *et al.* 2001).

Two critical points in this approach are associated with the boundary condition at the top of the atmosphere and truncation effects in the variational method with respect to the number of test functions used to represent the normal modes solution. In practice, the normal modes are computed for an atmosphere model with a top boundary (550 km) high enough to almost fully damp the modeled normal modes. The more rigorous boundary condition of elastogravity atmospheric waves proposed by Watada (2009) is naturally accounted for and the free-surface boundary condition is kept for normal modes computations. The variational techniques used for the complex normal mode computation is therefore almost identical to the Galerkin computation, used extensively for computing solid Earth normal modes (Park & Gilbert 1986). Truncation effects are associated with the finite number of real normal modes (all with the same angular order, $\ell$, but a different radial number, $n$, used in the variational computation as test functions. The normal modes are computed using the 100 real normal modes nearest in frequency (but with the same $\ell$ order). Although viscosity effects (i.e. the term $\omega B$) can be computed directly when both the displacement and velocity are computed by the Galerkin method, a few additional iterations are carried out in order to fully model the frequency dependence of seismic velocities associated with the attenuation and physical dispersion in the solid part of the model [i.e. $\mathbf{A}(\omega)$], taken here as the classical constant Q in the PREM model (Dziewonski & Anderson 1981), but with the associated physical dispersion of seismic velocities.

## 3 ATMOSPHERIC RESONANCES OF THE TSUNAMI MODES

The modes are computed for the NRLMSISE-00 atmosphere for Hawaii at the local time of the tsunami's arrival, (i.e. 20°N, 155°W at 0:00 LT (10:00 UT), on 2012 October 28 and with the F10.7 index corresponding to that day (121.7 sfu). The local bathymetric data are from the General Bathymetric Chart of the Ocean with 30 arcsec resolution for a depth of 4750 m. Fig. 1 represents the dispersion diagram (eigenfrequency as a function of $\ell$) for normal modes computed by the MINOS software and used as input for the variational second step. There are three types of modes: solid modes (Rayleigh modes in green, noted R), ocean modes (tsunami modes in black, noted T) and atmospheric modes (gravity modes in red, noted G; Lamb modes in light blue, noted L; and acoustic modes in dark blue, noted A). For infinite ground rigidity and for the long wavelength waves ($kD \ll 1$), the tsunami phase velocity is constant and equal to $c_{\mathrm{tsunami}}^{\mathrm{phase}} = \sqrt{gD}$. Here, $k$ denotes the tsunami's wavenumber, $D$ the ocean depth and $g = 9.8\,\mathrm{ms}^{-2}$, the Earth's surface gravity. Note discontinuities in the normal modes branches at $\ell = 380$ due to the fact that we are using two starting models: one computed up to an altitude of 550 km for $\ell \leq 380$ and a second one for an altitude of 400 km for $\ell > 380$. Mode branches with marked discontinuities are associated with branches having significant energy above 400 km, while all the energy of those without

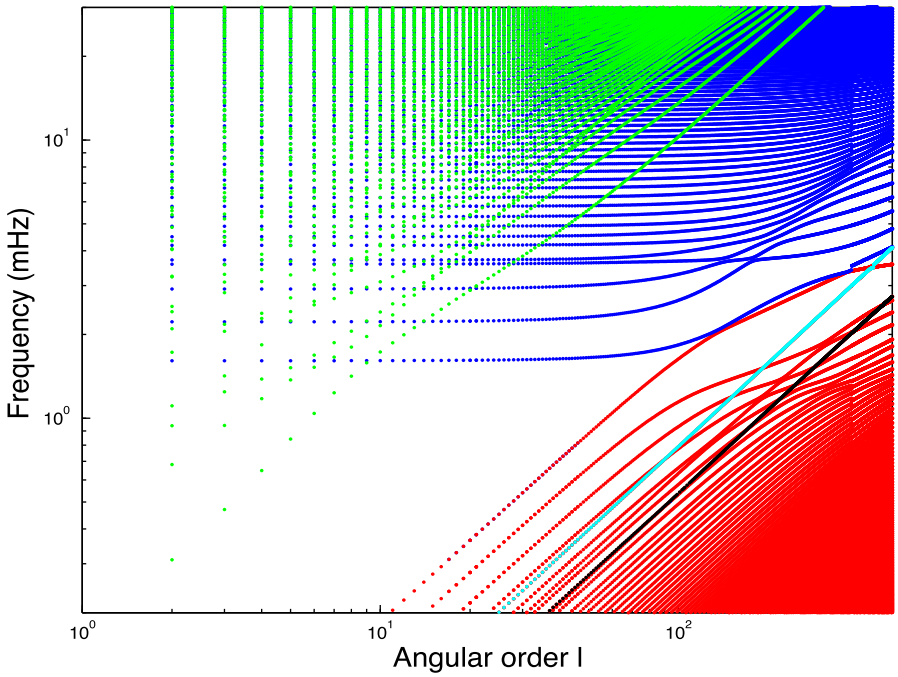


**Figure 1.** Dispersion of normal modes of the full Earth system for the 0.1–30 mHz frequency range. Atmospheric gravity modes (G) are plotted in red, Rayleigh modes (R) in green, atmospheric acoustic (A) modes in dark blue, Lamb modes in light blue (L) and tsunami modes (T) in black.

any significant discontinuities is below that altitude. Verifications carried out on the obtained solutions show that, no significant effect were found in the normal modes computation by changing the upper altitude of our model from 550 to 400 km for $\ell > 380$ as long as the normal modes are fully damped at 400 km. Rayleigh modes are subject to atmospheric resonances when their dispersion branch crosses the dispersion curves of the fundamental and overtones acoustic branches. The frequencies of the three clearly observed resonances (and crossing of dispersion curves) are near those of the fundamental (3.70 mHz and 4.5 mn), first (4.3 mHz and 3.9 mn) and second (5.0 mHz and 3.3 mn)× acoustic overtones. These resonances were observed in seismic records of the Pinatubo eruption, e.g. Kanamori & Mori (1992), Widmer & Zürn (1992) and Watada & Kanamori (2010) or in the continuous excitation of normal modes (Nishida 2000) and can be retrieved through the atmospheric coupling of normal modes (Lognonné *et al.* 1998). Similar resonances are found for tsunamis, when the tsunami branch crosses the atmospheric gravity mode branches.

In order to illustrate these resonances, we computed the distribution of the normal modes' energy in the ocean, solid Earth or atmospheric layers. Normal mode energy is proportional to:

$$P = \rho_0 \, |\mathbf{u}_\mathbf{k}|^2 \, . \tag{5}$$

The relative atmospheric energy of a mode is the ratio of the mode's energy integrated over the whole atmosphere by the mode's energy integrated over the whole Earth model. Similar definitions are used for relative energy in the solid Earth and ocean. The relative atmospheric energy of tsunami modes is shown for our case study in Fig. 2.

As may be expected, most of the energy of tsunami modes is in the ocean. The coupling between G and T modes is inversely proportional to the difference in the squared frequencies. The complex tsunami normal mode eigenfunction therefore has large atmospheric amplitudes. We shall later name this large atmospheric sensitivity as atmospheric resonance. In a similar way, the complex G modes close in frequency to T modes will have large amplitudes in the ocean.

This is illustrated by Fig. 2: in panel (a), there is a resonance when the T branch (black) crosses the G branches (red). Part of the tsunami energy from the ocean is transferred to the atmosphere (Fig. 2b). The resonances occur around 1.5 mHz (11.1 mn), 2 mHz (8.3 mn) and 2.5 mHz (6.7 mn). As attenuation is larger in the atmosphere than in the ocean, the quality factor is significantly reduced at resonance frequencies (Fig. 2c). However, due to the high value of the quality factor (up to $10^5$–$10^6$), the atmospheric effect on the quality factor is not likely to be observed in data, as these $Q$ factors correspond to a much longer propagation time than needed for trans-Pacific propagation.

The resonances at 2 and 2.5 mHz have interesting features. At these frequencies, we find that the tsunami's energy is almost equally distributed between the air and the ocean. These resonances occur in a very narrow frequency bandwidth and are similar to the ocean's anomalous transparency, an idea proposed by Godin (2006).

Let us now discuss some features of the tsunami normal modes eigenfunctions. In the atmosphere, the tsunami normal modes amplitude corresponds to gravity waves amplitude forced by the tsunami (IGWs). Let us remind that IGWs are characterized by the same horizontal wavenumber and frequency as tsunami waves. Furthermore, both the wave equation in the atmosphere and all boundary conditions between the ocean and atmosphere have to be met. Although our normal modes accurately verify these equations, including mass redistribution and compressibility aspects, the simplified gravity waves equation for an incompressible atmosphere can be used to understand the main feature of tsunami normal modes in the atmosphere. Let us recall that in this simple approach, the waves' propagation properties are determined by the Brunt–Väisälä (angular) frequency $N$, which is expressed as:

$$N^2 = -\frac{g}{\rho}\frac{d\rho}{dr} - \frac{g^2}{c^2}. \tag{6}$$

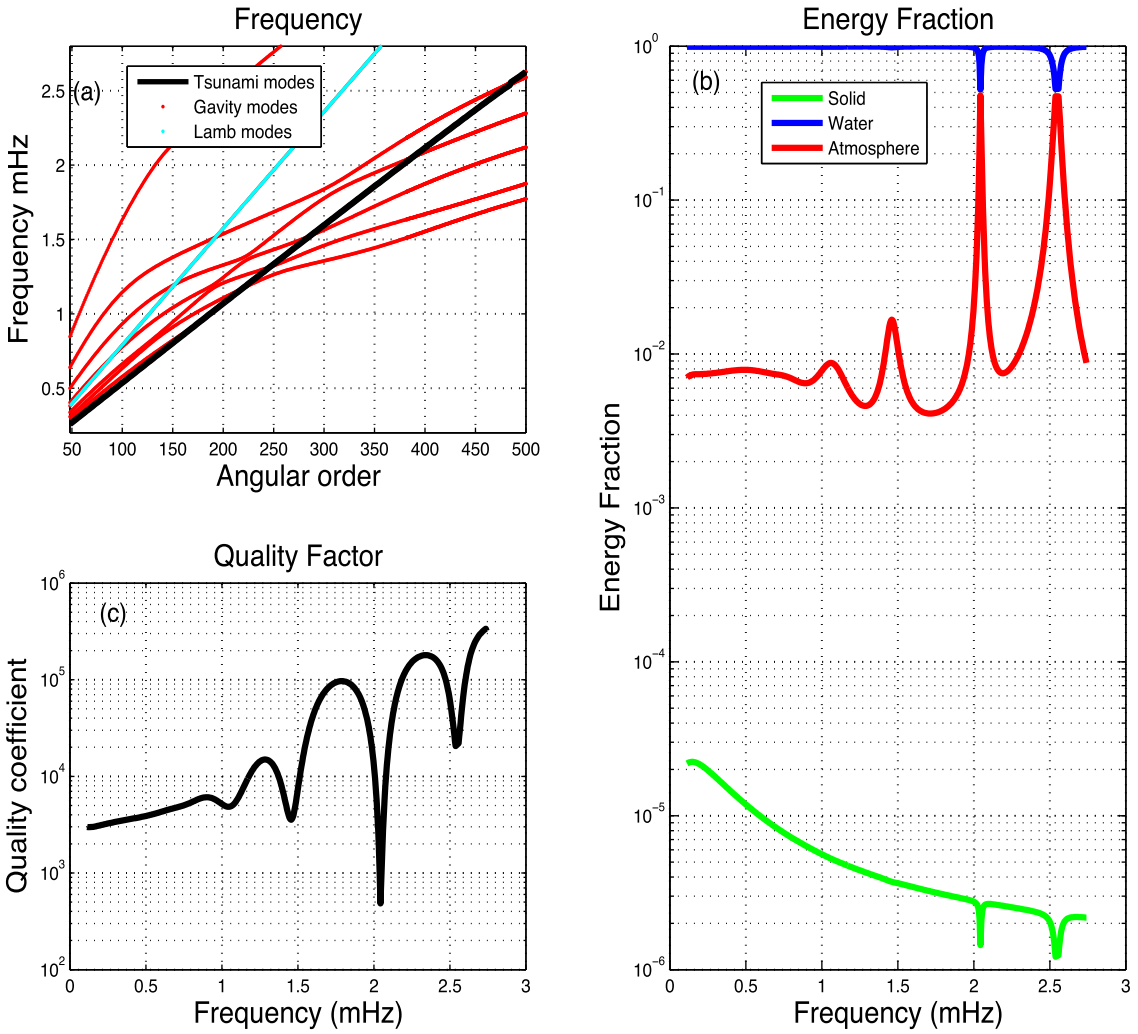


**Figure 2.** Tsunami normal modes resonances for an ocean depth of 4750 m. Three resonances occur at 1.5, 2 and 2.5 mHz. Panel (a): dispersion diagram centred on the tsunami branch. Panel (b): relative energy of the tsunami modes in the solid part (green), in the atmosphere (red) and in the ocean (blue). Note that here the tsunami's energy is almost equally distributed between the air and the ocean at 2 and 2.5 mHz. Panel (c): effect of the tsunami normal modes resonances on the tsunami quality factor.

When the Brunt–Väisälä frequency is greater than the modes' eigenfrequency, it is a gravity regime and gravity waves can propagate upward. Above this frequency, the mode is evanescent and decays exponentially with altitude. Note furthermore that compressibility is fully accounted for in our normal mode modeling, unlike in some previous models (Occhipinti *et al.* 2008) which were made for an incompressible atmosphere. Compressibility reduces the Brunt–Väisälä frequency and therefore increases the wavelength of the tsunami normal modes in the atmosphere or even makes them evanescent. The dispersion relationship of the gravity waves is then expressed as:

$$m^2 = k^2 \left[ \frac{N^2}{\omega^2} - 1 \right], \tag{7}$$

where $m$ is the vertical component of the wavenumber, $k$ the horizontal component and $\omega$ its frequency. Here, the gravity waves are forced by the tsunami, so the relationship between $\omega$ and $k$ is imposed by the tsunami:

$$\omega = k\sqrt{gD}. \tag{8}$$

Let us remember that $k = \frac{2\pi}{\lambda_{\rm tsu}}$ and $m = \frac{2\pi}{\lambda_V}$ where $\lambda_{\rm tsu}$ and $\lambda_V$ are the tsunami horizontal wavelength and tsunami atmospheric vertical wavelength, respectively. Finally, the vertical wavelength of the tsunami mode in the atmosphere can be written as:

$$\lambda_V = \frac{\lambda_{\rm tsu}}{\sqrt{\frac{N^2}{\omega^2} - 1}}. \tag{9}$$

For frequencies above the Brunt–Väisälä frequency, $\lambda_V$ is imaginary and gives us the damping length. Below, $\lambda_V$ is the propagation wavelength in the atmosphere. Let us now interpret the amplitude of the normal modes with this wavelength.

Fig. 3 shows the complex eigenfunctions of the T modes for resonances at 1.5, 2 and 2.5 mHz along with the associated Väisälä frequency and vertical wavelength. Throughout the paper, the normal modes eigenfunctions $U_r(r)$ (vertical component) and $V_r(r)$ (horizontal component) are plotted on figures with an amplitude scaled by the inverse square root of the density. In the Brunt–Väisälä frequency panel, the mode's eigenfrequency is indicated by the vertical red line. The blue and green bars are respectively the minimum and maximum wavelength found with relationship (9). We define as a 'gravity waveguide' the propagation zone of

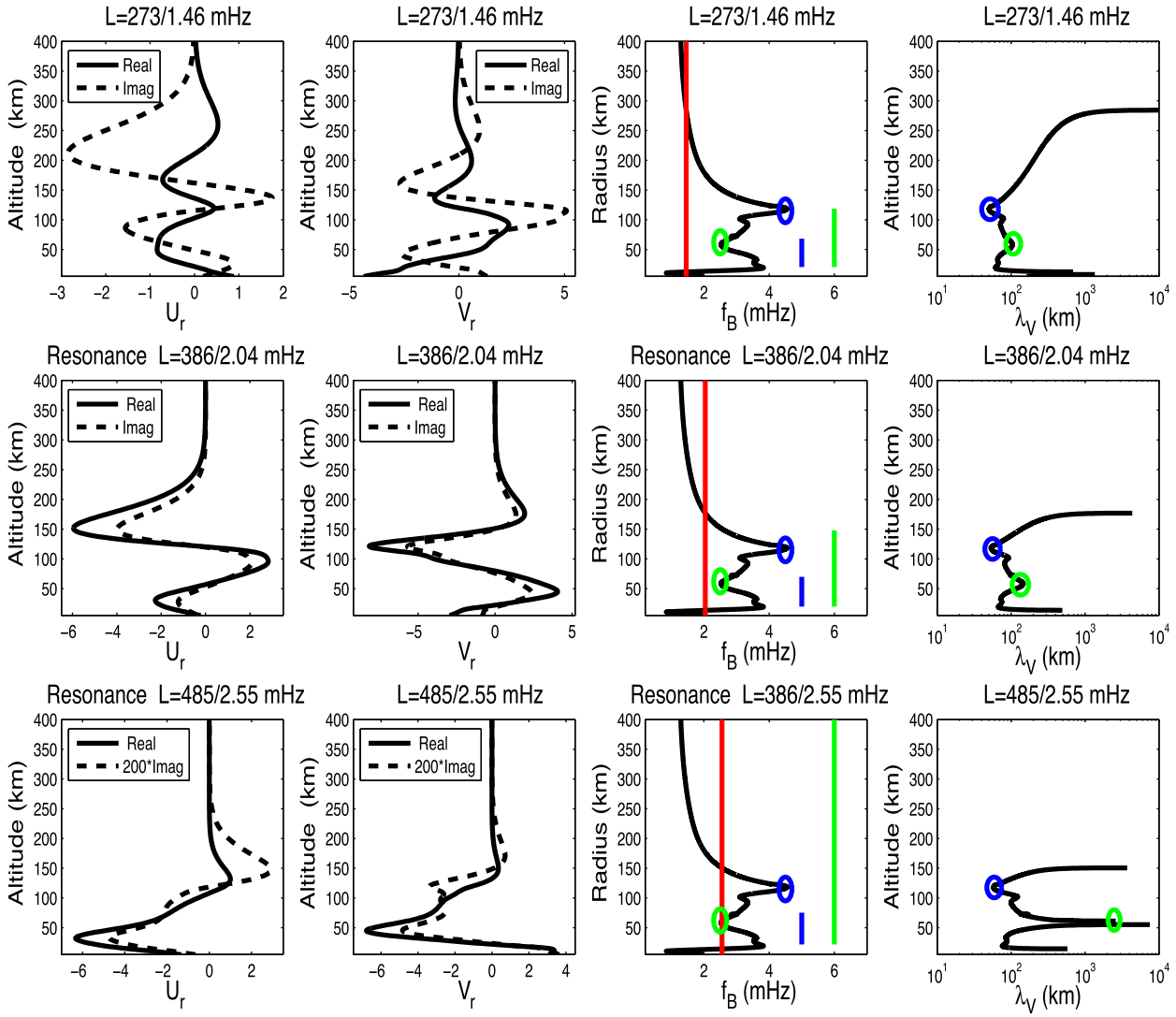


**Figure 3.** Propagation characteristics of the three resonant modes. From left to right: amplitude of the atmospheric part of vertical ($U_r$) and horizontal ($V_r$) normal modes eigenfunctions, scaled by the inverse square root of density, Brunt–Väisälä frequency ($f_B$) and vertical wavelength $\lambda_V$ as a function of the altitude for the 1.5, 2 and 2.5 mHz resonances from top to bottom. In the Brunt–Väisälä frequency panel, the resonant mode eigenfrequency is plotted with a red vertical bar, and the blue and green vertical bars are the minimum and maximum vertical wavelengths, respectively. The green and blue circles in the Brunt–Väisälä and vertical wavelength panels represent the location of the maximum and minimum of the vertical wavelength, respectively.

the atmosphere where the normal mode frequency is greater than the Brunt–Väisälä frequency. The height of the gravity waveguide, $h_{GW}$, ranges from 300 km at 1.5 mHz to 150 km at 2.5 mHz. For the first resonance, the gravity waveguide height is about 2.5 times larger than the maximum vertical wavelength, allowing wave oscillations in the atmosphere. This propagative character is found in the $\pi/2$ phase shift between the real and imaginary parts of the normal mode. The decrease in the real and imaginary parts' amplitudes above 200 km is due to the low density, which increases kinematic viscosity. At a height of 285 km, the Brunt–Väisälä frequency is below 1.5 mHz and the mode starts to be evanescent: its amplitude then decays very rapidly with height, as both the atmospheric cut-off and viscosity are concurring to damp the amplitude. The amplitude of the mode nevertheless remains large at the $F_2$ peak altitude (around 300 km), which explains why big signals are observed at 1.5 mHz in the tsunami-induced perturbed TEC spectrum (Rolland *et al.* 2010).

The amplitudes at ionospheric heights are much lower in the case of the higher frequency normal modes (i.e. 2 and 2.5 mHz) and become almost null at an altitude of 300 km. This is due to the evanescent property of the wave and not to atmospheric viscosity. Above 2 mHz, viscosity plays a minor role in the normal mode decay, which is instead mainly related to atmospheric cut-off. Furthermore, the value of the mode's vertical wavelength in the atmosphere is much higher and for the 2 mHz resonant mode about 2 oscillations are accommodated in the atmospheric waveguide. In this case, the vertical wavelength and the waveguide height are comparable, leading to a critical configuration where the real part and imaginary amplitudes are in phase. At 2.5 mHz, the maximum vertical wavelength value is so high (more than 1000 km) that the mode only has one evanescent damping effect and is little affected by viscosity. In the latter case, the imaginary part of the mode is much smaller than the real part (note that the imaginary part of the 2.5 mHz normal mode has been multiplied by 200).

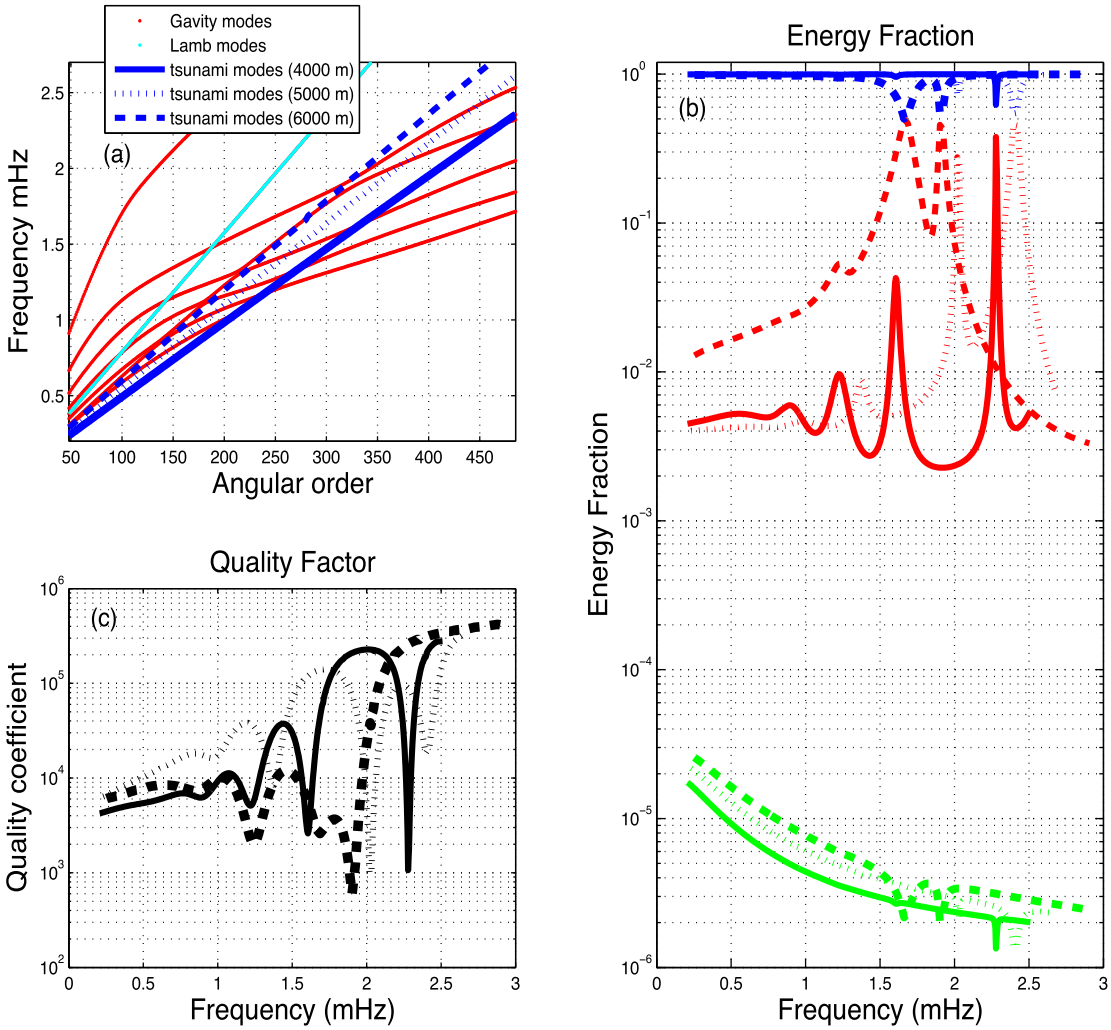


**Figure 4.** Panel (a) shows the dispersion diagram of the tsunami branches, with ocean depths of 4, 5, and 6 km in addition to the Lamb and atmospheric gravity modes. Panel (b) shows the energy fraction in the atmosphere, ocean and ground, with resonance peaks. The blue, red and green curves stand for the ocean, atmosphere and solid energy fraction, respectively. Panel (c) shows the tsunami quality factor plotted as a function of frequency. The tsunami mode's phase velocity and therefore the resonance frequencies depend on the ocean depth.

Both the limited number of oscillations of the tsunami normal mode amplitude as a function of altitude and the evanescent transition explain the similarities in the waveform of ionospheric TEC signals and that of water height signals, as illustrated by several observations (Rolland *et al.* 2010; Kherani *et al.* 2016).

The atmospheric coupling of a tsunami mode depends however not only on the structure of the atmosphere, in a similar way to the coupling of Rayleigh waves (Rolland *et al.* 2011b), but also on ocean depth, which determines the phase velocity of the tsunami branch and therefore coupling with the atmospheric branches. This sensitivity to atmospheric and oceanic structure is analysed in the following section.

## 4 SENSITIVITY TO OCEAN DEPTH

We computed the modes up to $\ell = 500$ for three ocean depths (4, 5 and 6 km). The atmospheric model of the Haida Gwaii case was used. Fig. 4 shows the resulting dispersion diagram, energy fraction and quality factor. Atmospheric gravity branches are not affected by ocean depth changes. Note that this figure only shows those crossing the tsunami branch and responsible for atmospheric resonances. All the others were nevertheless used for the variational computation of the tsunami modes described in Section 2. As the phase and group velocity of the tsunami waves depend on $\sqrt{D}$, a 1 km change in the ocean depth markedly shifts the atmospheric resonance frequency. This bathymetric variation also affects the transfer of energy between the ocean and solid part as shown in Table 1. Indeed, for an ocean depth of 4 and 5 km, the tsunami branch just cuts across the gravity branches and the only major coupling occurs for modes with frequencies close to the resonance. For a 6 km depth, on the other hand, the tsunami branch is almost parallel to one of the gravity branches between 1 and 2 mHz. Major atmospheric couplings are thus found in this frequency bandwidth, as the group or phase velocities of the tsunami waves are quite close to those of the corresponding atmospheric gravity mode branch. More than 10 per cent of the tsunami's energy is then transferred to the atmosphere. This significant coupling is similar to the acoustic–gravity atmosphere–ocean coupling recently analysed by Godin *et al.* (2015) with an asymptotic approach that neglects the solid Earth part. This major coupling is shown in Fig. 5, where large amplitudes are found below 100 km for an ocean depth of 6 km.

**Table 1.** Eigenfrequency and energy fraction in the atmosphere and ocean for resonance at an ocean depth of 4000, 5000 and 6000 m.

| | 4000 m | | | 5000 m | | | 6000 m | | |
|---|---|---|---|---|---|---|---|---|---|
| Frequency (mHz) | 1.24 | 1.61 | 2.28 | 1.39 | 2.03 | 2.4 | 1.24 | 1.67 | 1.9 |
| Energy fraction in ocean | 0.99 | 0.96 | 0.62 | 0.94 | 0.72 | 0.55 | 0.95 | 0.51 | 0.58 |
| Energy fraction in atmosphere | $1.0 \times 10^{-2}$ | $4 \times 10^{-2}$ | 0.38 | $8.0 \times 10^{-3}$ | 0.26 | 0.45 | $5.2 \times 10^{-2}$ | 0.49 | 0.42 |

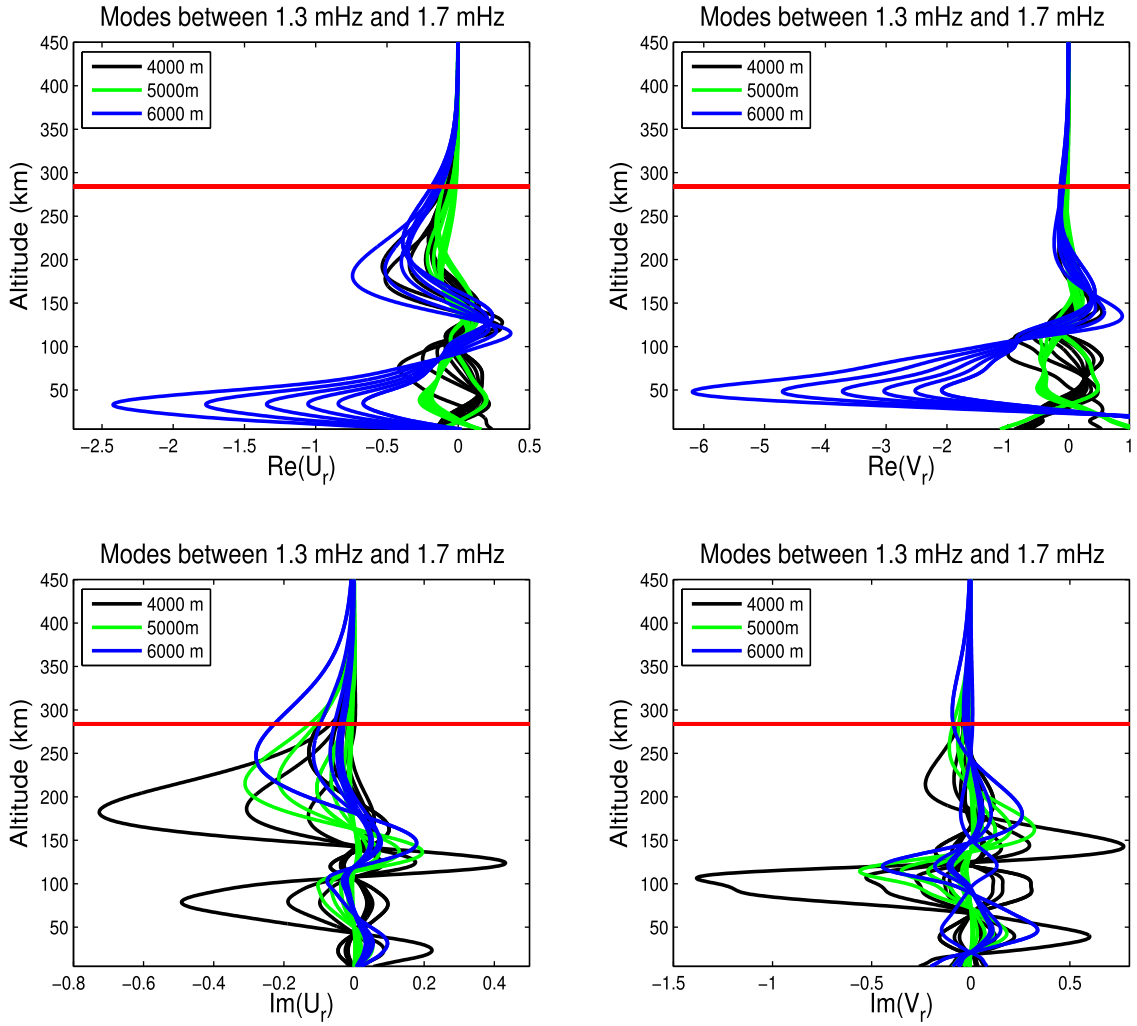


**Figure 5.** Amplitude of tsunami eigenfunctions between 1.3 and 1.7 mHz in the atmosphere for three different ocean depths. The red horizontal bar represents the upper altitude limit up to which the 1.5 mHz mode can propagate. The modes for a 6 km ocean depth are highly resonant only at low altitudes (below 60 km).

In the previous section, we showed that the high-frequency modes above 2 mHz are evanescent above 200 km and do not contribute to marked thermospheric winds. Fig. 5 shows the vertical and horizontal components for 4, 5 and 6 km ocean depths and for frequencies between 1.3 and 1.7 mHz. The red horizontal line marks the altitude where the Brunt–Väisälä frequency reaches 1.5 mHz. It is clear that the large resonance observed in the energy for 6 km is corresponds to the large low-altitude amplitudes, below 60 km. This high-frequency resonance will have little effect on the TEC, as the normal mode amplitudes are small in the ionosphere. Indeed, already at the $F_2$ peak altitude (300 km), the wave is attenuated by a factor of 4–5. At this altitude, the amplitude of the modes between the 4 and 6 km depths is similar. For the 5 km ocean depth, the amplitude of the wave is smaller.

## 5 SENSITIVITY TO LOCAL TIME

In order to analyse the sensitivity of normal modes amplitude to local time, we computed the normal modes while changing just the local time, and keeping all other parameters (day and location) as in Section 3 and for local ocean depth equal to 5 km. The four different local times chosen are 00:00, 06:00, 12:00 and 18:00. Fig. 6 shows the vertical profiles of kinematic viscosity, air density, speed of sound and Brunt–Väisälä frequency for these different local times. These parameters are the most sensitive to solar radiation at higher altitudes. The energy fraction and quality factor for these four local times are shown in Fig. 7. Three resonances occurred around 1.4, 2 and 2.4 mHz. The phase velocity of the tsunami modes was found to depend only on the ocean depth and be unaffected by the variation in

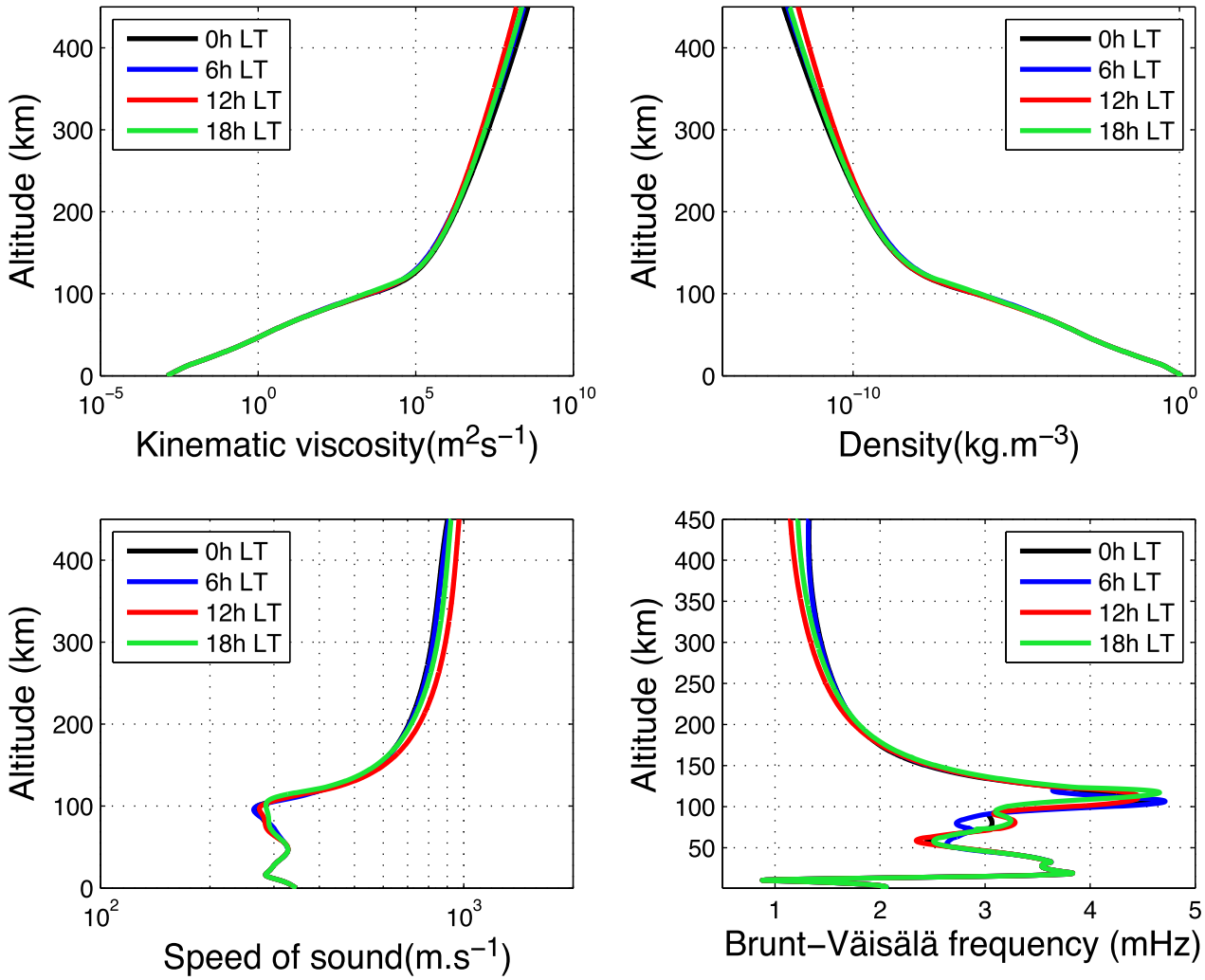


**Figure 6.** Atmospheric parameters (viscosity, density, speed of sound and Brunt–Väisälä frequency) for four different local times (00:00, 06:00, 12:00 and 18:00 LT) on 2012 October 28 as computed by the NRLMSISE-00 empirical model (Picone *et al.* 2002). The density and speed of sound are greater during the daytime, while viscosity and Brunt–Väisälä frequency are greater during the night-time. Sensitivity to the local time increases with altitude.

local time. However, the gravity waves' dispersion branches moved slightly as atmospheric parameters changed with local time. This explains the slight shift in resonance frequencies depending on local time. Variations in the energy fractions were also observed. Indeed, coupling strength increased when the waves' phase velocities were closer together. The relative sensitivity to the local time decreased at high frequencies. It was especially visible in the atmospheric energy fraction at 2.4 mHz. Indeed, as explained in Section 3, the normal mode at 2.4 mHz is already evanescent at 150 km, and cannot be affected by the temperature change in the thermosphere (and therefore by density and sound speed changes) as much as the modes propagating widely in the thermosphere. As there is smaller variation in the atmospheric parameter below 200 km, the sensitivity to local time is lower. The complex eigenfunctions of the resonance at 1.4 mHz are shown in Fig. 8. The horizontal lines represent the upper limit of the wave's propagation regime, defined as the altitude where the frequency equals the Brunt–Väisälä frequency. This upper limit varies from 275 km at noon to 323 km at mid-night. It is clear that there is a daytime regime and a night-time regime.

At low altitudes, the real part of the mode is not very sensitive to local time due to the small variation in the atmospheric parameters below 100 km. At higher altitudes, there is a major difference in amplitude and phase shift, as a consequence of the variation in altitude of the evanescence threshold for these modes. The real and imaginary parts of the normal mode amplitudes are in phase and mostly dictated by the variation in viscosity depending on local time. As for Rayleigh modes, atmospheric amplitudes for the 1.5 mHz resonance are larger during the daytime than during the night-time, due to the higher density and lower viscosity at ionospheric heights (Rolland *et al.* 2011a). Furthermore, the ionosphere is more developed during the day. We can therefore expect the electron density signals during the daytime to be much greater due to the combination of larger driving neutral atmospheric waves and a higher density of transported electrons.

## 6 NORMAL MODES SUMMATION FROM SEAFLOOR TO IONOSPHERE

While the amplitude of normal modes is already useful to explain the mechanism of the atmospheric–ocean coupling of tsunamis, it is even more suitable for modeling the response anywhere in the Earth to any source that excites these normal modes, whether they are earthquakes, tsunamis or volcanic eruptions for instance. The

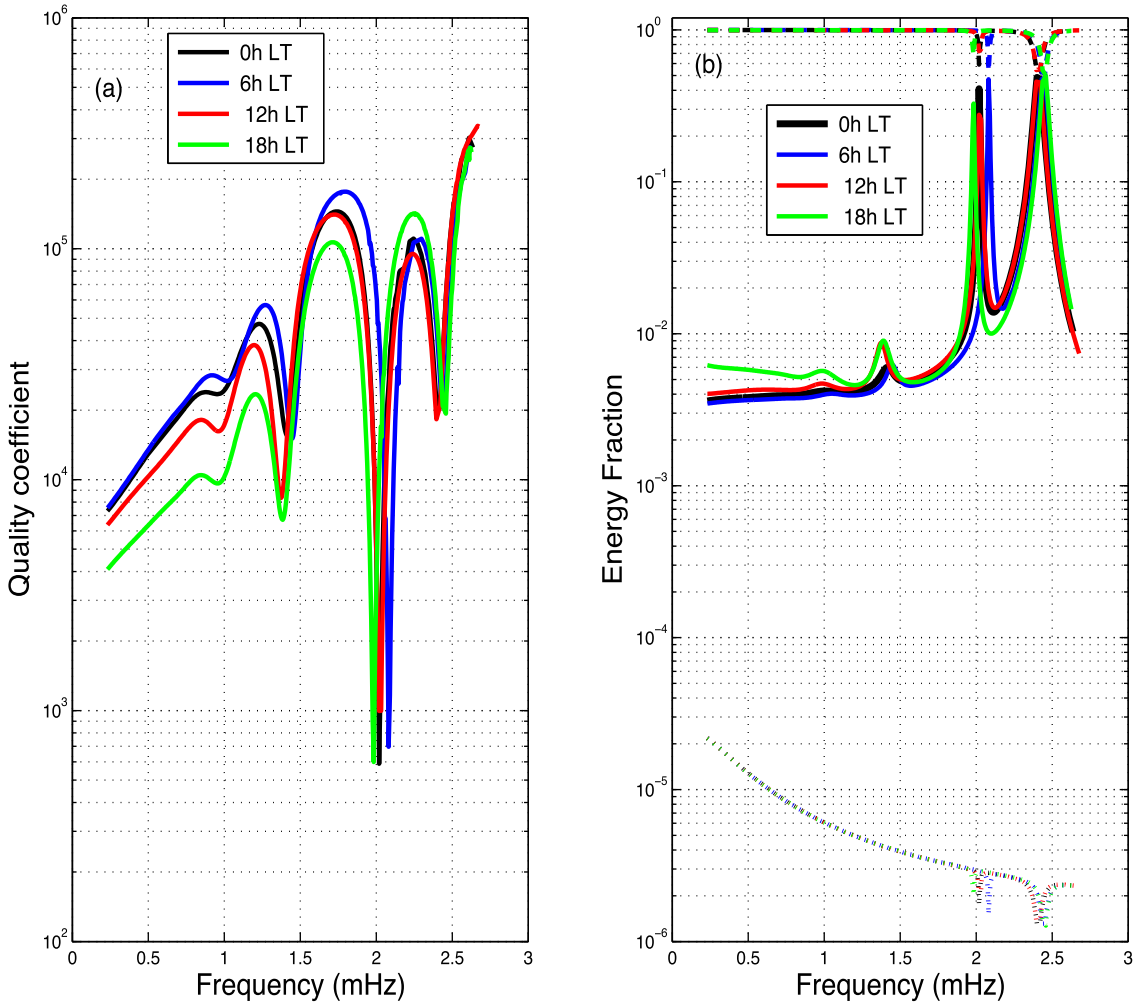


**Figure 7.** Variability of tsunami modes resonance in the atmosphere depending on local time. (a) Quality factor as a function of frequency for 00:00, 06:00, 12:00h and 18:00 LT. (b) Energy fraction as a function of frequency in the atmosphere (solid line), ocean (dashed line) and solid Earth (dotted line). Sensitivity to the local time is higher for low frequencies due to the large variations in temperature and density at high altitudes.

normal mode summation technique is extensively used in seismology. Normal mode summation can also be used to compute the solid Earth's response to a tsunami [e.g. ground tilt, see Yuan *et al.* (2005)], or the ocean's response [e.g. water height variation from DARTs (Titov *et al.* 2005); atmospheric wind perturbation (Garcia *et al.* 2014)] or ionospheric perturbations, in the latter case by applying the transfer function from the neutral perturbation to the electron density perturbation (Coïsson *et al.* 2015).

In order to compute the displacement or velocity, we use the normal mode summation expression given by Lognonné (1991):

$$\mathbf{s}(\mathbf{r}, t) = H(t)\mathrm{Re}\left[\Sigma_k\, \mathbf{M} : \epsilon_k(\mathbf{r}_0)\, \mathbf{u_k}(\mathbf{r}) \frac{1 - e^{i\omega_k t}}{\omega_k^2}\right], \qquad (10)$$

where $\mathbf{M}$ denotes the moment tensor, $\boldsymbol{\epsilon}$ the normal mode strain at the epicentre $\mathbf{r}_0$, $H(t)$ the Heaviside function, $\mathbf{u}_k(\mathbf{r})$ and $\omega_k$ the normal mode displacement function at location $\mathbf{r}$ and eigenfrequency, respectively and $k$ the normal mode index.

To further compute the TEC perturbation induced by tsunamis from the atmospheric wind field, we use the methods of Rolland *et al.* (2011b) and Coïsson *et al.* (2015). Fig. 9 shows the models reconstructed using such a normal mode summation technique for the vertical TEC, and for vertical and horizontal displacements of the neutral atmosphere at altitudes of 300, 200 and 0 km (interface between the ocean and the atmosphere) and at a depth of 5 km (interface between the ocean and the Earth's crust). A point source model was used with the centroid moment tensor (CMT) of the Haida Gwaii tsunami in 2012 of magnitude $M_w = 7.8$. As in all normal modes summations seismograms, ringing are present in the displacement seismograms, especially before the expected first arrival, as the summation is limited to only one branch. This feature is comparable to the ringing of Rayleigh waves summation (e.g. Artru *et al.* 2004), when only the fundamental spheroidal branch is modeled. Note however that the ringing is strongly attenuated on the TEC synthetics, as the later is based on the integrated signal and therefore is low pass filtered by the measurement.

The waveforms of Fig. 9 show the main features of tsunami propagation and the differences with the incompressible shallow water solution.

The horizontal displacement between the surface and the bottom of the ocean is almost identical, the small difference being mostly associated with water compressibility. The dispersion of tsunamis waves related to both the coupling with the ground and compressibility of water (Watada *et al.* 2014) is also shown, associated with the ramp starting about 20 min prior to the tsunami's first arrival. This coupling with the solid Earth generates a non-zero vertical displacement at the bottom of the ocean of about 0.5 per cent of the

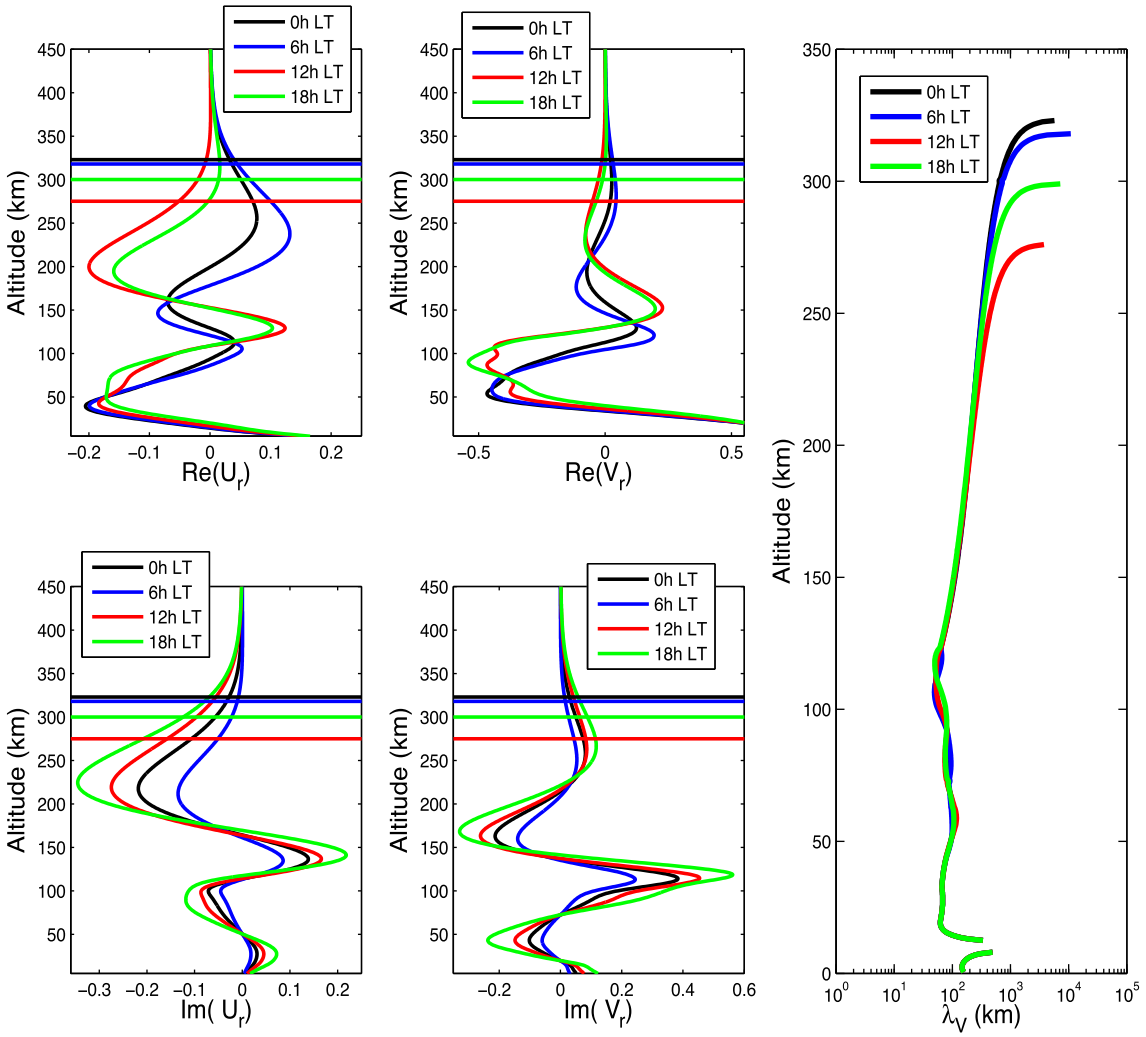


**Figure 8.** Tsunami eigenfunction in the atmosphere at 1.5 mHz for the four different local times. The horizontal lines correspond to the upper limit of the propagation zone for the tsunami modes. The vertical wavelength of the mode is plotted on the right-hand panel. A daytime and night-time regime can be clearly identified.

tsunami height for the PREM crust elastic properties, and about 0.02 per cent for the horizontal amplitude at the solid side of the ocean bottom interface. The tsunami's horizontal and vertical displacements are in quadrature phase as expected from the theory (see Appendix for further details). Note that the horizontal to vertical displacement ratio in the atmosphere depends, for a given horizontal wave number or angular order, on the vertical amplitude just above the sea surface and of the tsunami phase velocity. This ratio is therefore slightly affected by the atmospheric coupling of the tsunami, especially near the resonances where we have $Q$ as low as about 500 for the 2 mHz resonance. It might lead to the generation of not only tsunami-induced gravity waves but also to atmospheric gravity waves not representative of a realistic tsunami-equivalent source but present only due to the non-explicit integration of the tsunami atmospheric coupling.

At the ocean surface, the vertical displacement is continuous between the ocean/atmosphere interfaces. Nevertheless, the horizontal displacement is almost opposite, with a $\pi$ phase shift. Indeed, when the surface of the water moves forward, the air slides over it to fill the vacuum left by the displaced water mass. This is a classical feature of an internal mode in a two-layered fluid system under gravity (Massel 2015). Adding the atmosphere slightly increases the amplitude of this precursor on the horizontal component as well as on the solid response at the bottom of the ocean, and needs to be taken into account in order to accurately model the tilt generated by tsunamis (e.g. Boudin *et al.* 2013).

Above the surface, upward propagation is illustrated with the waveforms at an altitude of 200 and 300 km. At 200 km, upward propagation is more complex, with significant signals after the main wave's arrival, probably related to the dispersion of the rising wave. At 300 km, however, the signal looks like a low-pass filtered water height waveform. This can be interpreted as a direct consequence of the transition from propagation to evanescent modes. There is clearly a delay in the first wave's arrival time due to propagation from the bottom of the atmosphere up to an altitude of 300 km (around 7 min, consistent with the analysis of Occhipinti *et al.* 2013).

Last but not least, the vertical peak-to-zero displacement amplitude of about 5 cm at sea level is magnified as altitude increases, reaching a few dozen kilometres at 300 km, typical of the $10^5$ amplification factors expected for these long-period waves.

In conclusion, normal mode summation provides a complete and accurate description for both the vertical and horizontal neutral winds. This technique can be used to model ionospheric signals through neutral wind–plasma coupling. Modeling results can then

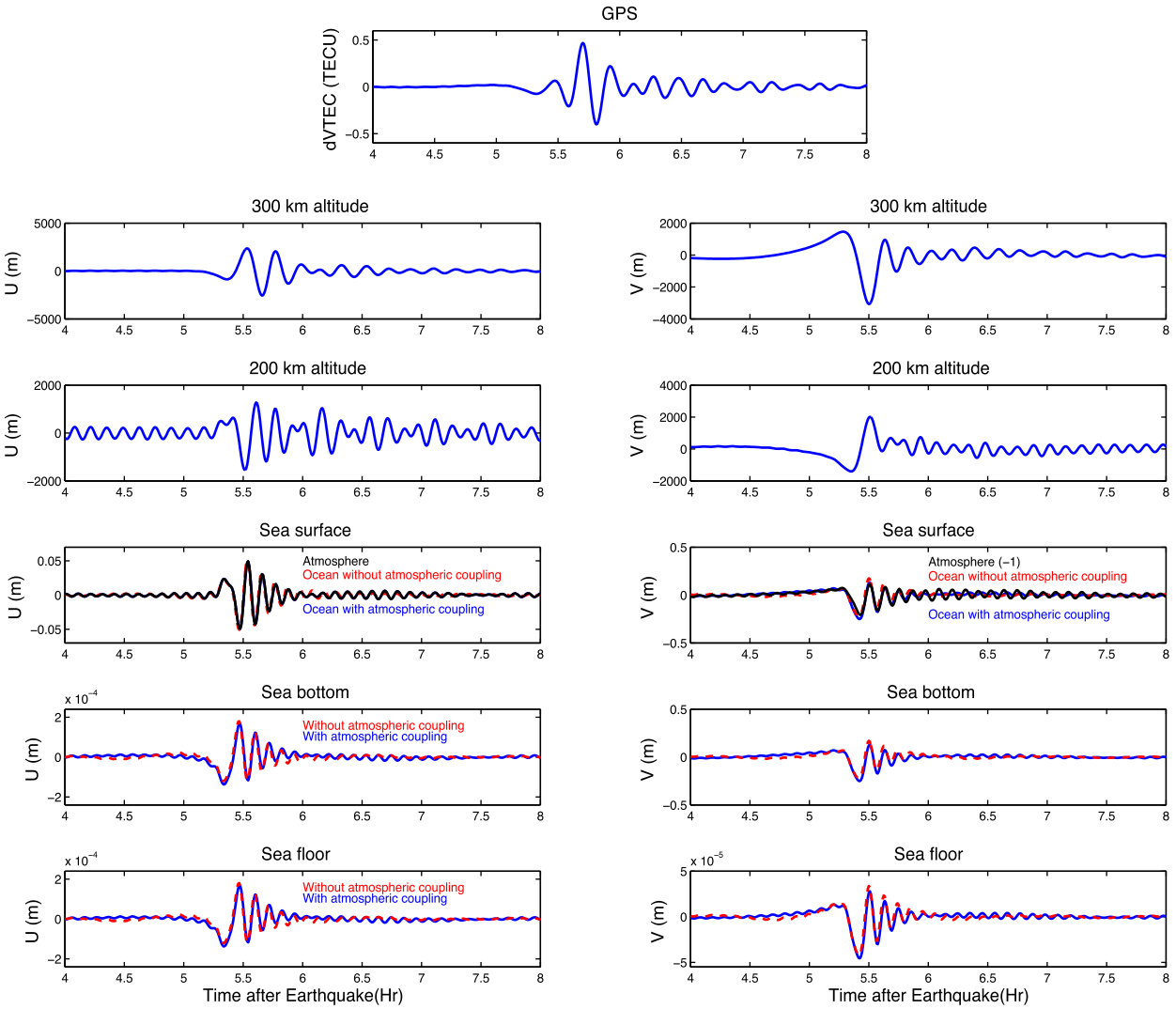


**Figure 9.** Tsunami-induced displacement in the ocean, the neutral atmosphere and the ionosphere. From bottom to top: modeled vertical (left-hand side) and horizontal displacement (right-hand side) at the seafloor, sea bottom, sea surface, in the atmosphere (at 200 and 300 km), and ionosphere (GPS TEC) for the Haida Gwaii study case, computed at the location of the DART buoy 51407 using the CMT Harvard source.

be compared to observations, as is the case later in this paper for several different tsunamis.

## 7 GRAVITY MODES AND LAMB WAVES; EARLY ATMOSPHERIC GRAVITY WAVE ARRIVALS

As observed after the Tohoku earthquake, underwater earthquakes not only generate tsunamis but also gravity waves (Rolland *et al.* 2011a; Komjathy *et al.* 2012; Yu *et al.* 2015). We therefore develop first the coupling properties of the atmospheric gravity and Lamb modes with the ocean before computing the waveforms of the associated branches.

### 7.1 Atmospheric gravity modes resonances with the ocean

When the atmospheric gravity branches cross the tsunami branch, there is resonance with the ocean structure as shown in Fig. 10 for the gravity fundamental and the first two overtone branches. These resonances occur around 1.5, 2 and 2.5 mHz, as for tsunamis. At these frequencies, part of the energy is efficiently transferred from the atmosphere to the ocean [panel (c)]. We label these modes with the increasing number of zero crossing between the tropopause and about 150 km of altitude, which corresponds to the altitude range where the Brunt–Väisälä frequency is larger than the mode frequency. The fundamental mode is therefore the 2.5 mHz one, while the first and second harmonics are the 2 and 1.5 mHz modes. For the 2 and 2.5 mHz resonances, energies in the atmosphere and ocean are comparable. These resonance features can also be found in the quality factor, which shows a local maximum at the resonance frequencies due to the fact that water attenuates much less than the atmosphere. On the contrary, a local $Q$ minimum is found for resonances with fewer trapped gravity waves. As the L branch does not cross the T branch (panel a), there is no resonance for Lamb modes, which have almost no energy in the ocean (panel c). The surface trapping of Lamb waves make them undetectable in the ionosphere.

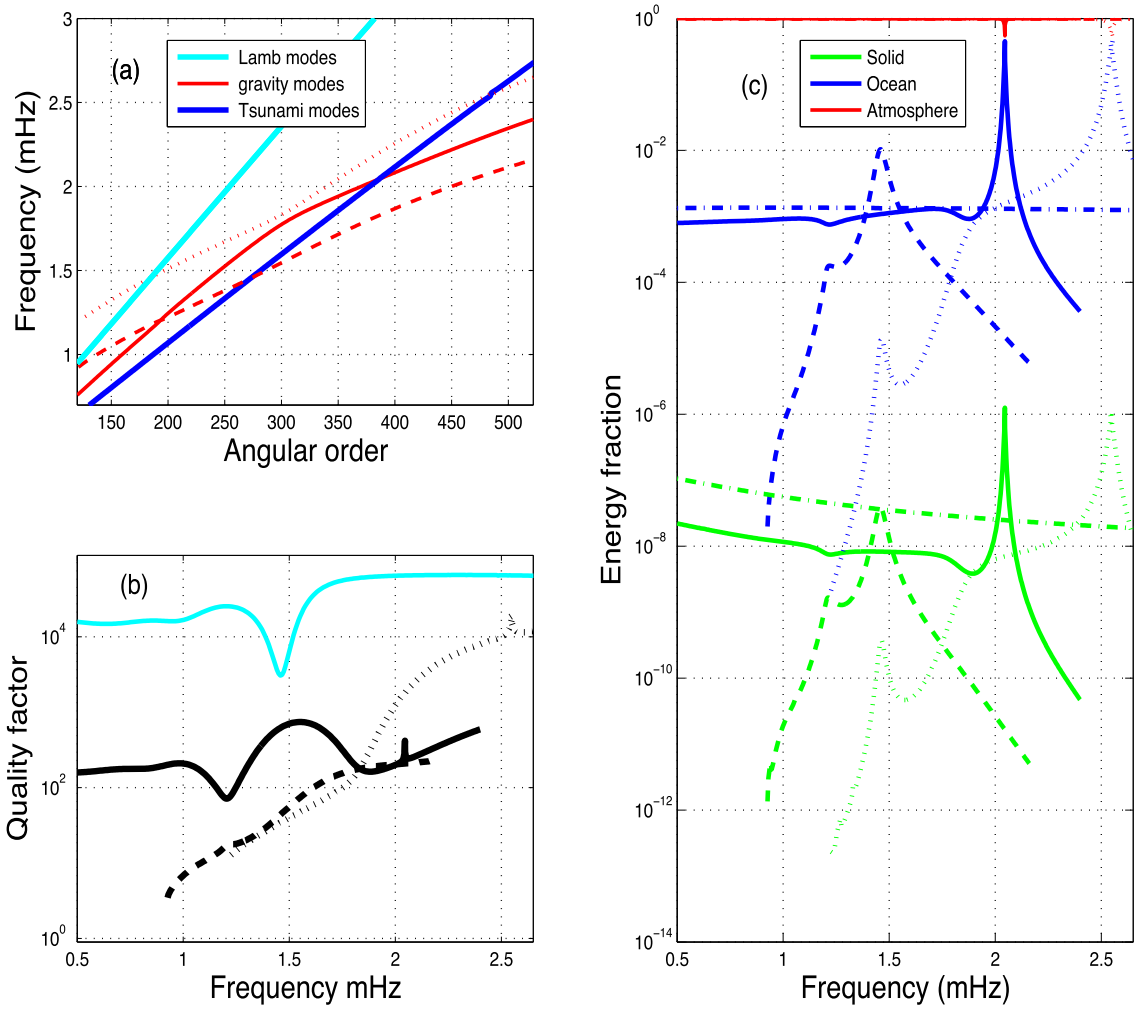


**Figure 10.** Gravity normal modes resonances for an ocean depth of 4750 m. Oceanic resonance in the fundamental G modes (respectively solid, dashed and dotted lines) with the T modes. In (a) and (b), the light blue solid line corresponds to the L modes. In (c), the Lamb branch is represented by dashed–dotted lines.

### 7.2 Fundamental gravity modes and tsunami precursors

The fundamental gravity mode branch is the only one with group velocities faster than those of the tsunami for frequencies below 1.6 mHz. This is illustrated by Fig. 11, which shows the variation in group velocity as a function of frequency for the L, G and T modes and for three different modeling assumptions.

The first is the classical approach, which assumes an incompressible oceanic layer (Okal 1988) for which phase and group velocities are, respectively:

$$c(\omega) = \sqrt{\frac{gD\tanh(k(\omega)D)}{k(\omega)D}}. \tag{11}$$

$$u(\omega) = c(\omega)\left[\frac{1}{2} + \frac{k(\omega)D}{\sinh(2k(\omega)D)}\right]. \tag{12}$$

The second is the tsunami normal mode computation for PREM without atmosphere, which can be directly compared to Watada *et al.* (2014). The third, and last, is the computation with both the solid part and the atmosphere, as described above. At 2 and 2.5 mHz, significant variations are observed for the tsunami group velocity. These perturbations cannot be seen in the model without the atmosphere, suggesting that they are due to atmospheric resonance by gravity waves. At these frequencies, the fundamental and the first overtone G modes show a peak in group velocity which corresponds to oceanic resonance.

As the modes below 1.6 mHz have larger group velocities than the tsunami, the fundamental gravity wave below 1.6 mHz should arrive before the tsunami. We illustrate this phenomenon with modeled seismograms computed at the ocean surface and in the atmosphere (Fig. 12) for both tsunami and fundamental gravity branches and for two tsunamis: the 2011 Tohoku tsunami and the Haida Gwaii tsunami. Results are summarized in Fig. 12.

The result shows the perturbations in electron density and neutral displacement at 260 km and the sea level displacement for both the tsunami and the fundamental gravity modes for the two tsunamis. The amplitude of the electron density perturbations is reported in Table 2 for all cases.

Let us set the detection threshold of the electron density perturbation to about $\delta n_e^{\text{threshold}} \approx 5 \times 10^9$ e m$^{-3}$, which corresponds to an integration over 50 km, to about 0.025 TECU and therefore to an amplitude comparable to the TEC perturbation noise level in Hawaii for the Haida Gwaii ionospheric TEC observations (Grawe & Makela 2015).

In Table 2, we reported the ionospheric perturbation induced by atmospheric gravity modes and tsunami modes in the case of

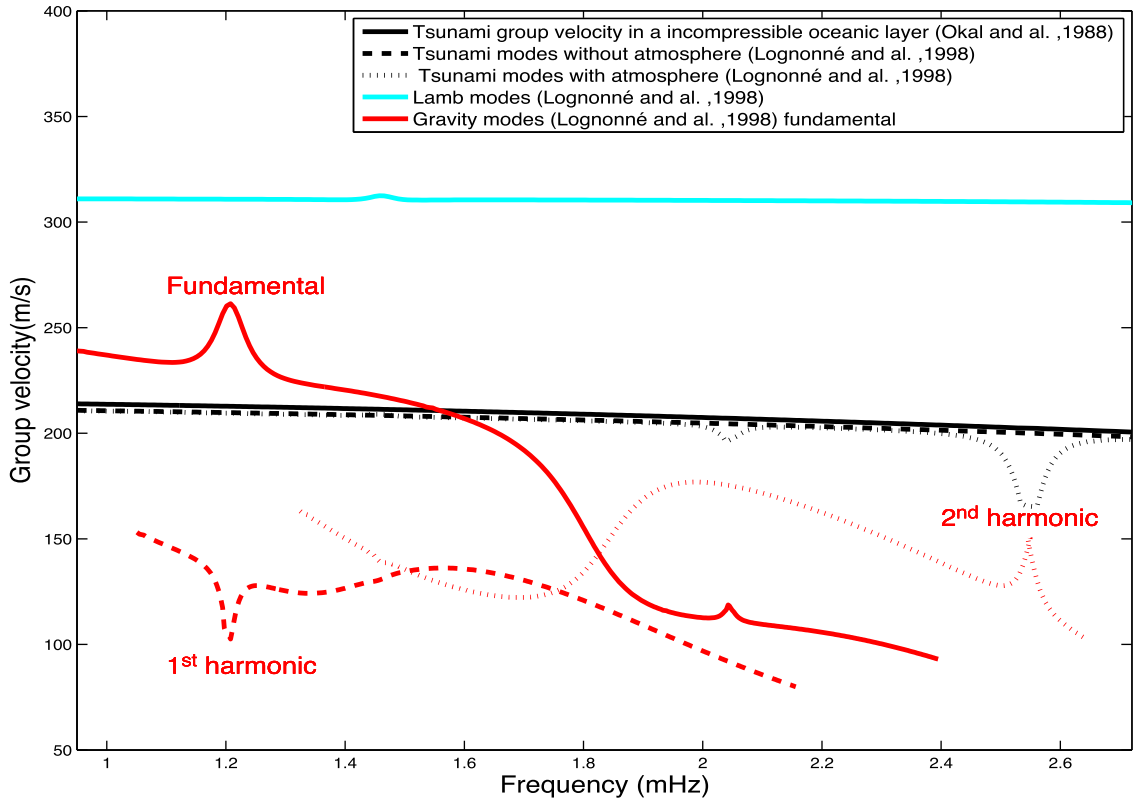


**Figure 11.** Group velocity of the L modes, G modes fundamental and two first overtones (red lines) and T modes (computed for three different physical assumptions). Note that below 1.6 mHz, the fundamental gravity waves travel faster than the tsunami. The ocean depth is 5 km.

the Tohoku and Haida Gwaii tsunami. The perturbation induced by the tsunami modes will be higher than the detection threshold for both events, however the ionospheric perturbation induced by gravity modes will be higher than the detection threshold only in the case of Tohoku. Indeed,the ionospheric perturbations for Haida Gwaii are six times smaller. This simple analysis suggests that the fundamental gravity waves generated at the source by the Tohoku quake have observable amplitudes and could be the waves preceding the Tohoku tsunami that were detected by Makela *et al.* (2011) off the Hawaiian shore. Future studies will have to be conducted in order to confirm this.

## 8 MODELING RESULTS AND COMPARISON WITH DATA

We now show modeling results for both the tsunami height and perturbed TEC for three different tsunamis. We first study the 2012 Haida Gwaii and 2006 Kuril Islands tsunami recorded off Hawaii. The corresponding ionospheric TEC observations were analysed by Grawe & Makela (2015) and Rolland *et al.* (2010), respectively. The third case is the large 2011 Tohoku tsunami (Kherani *et al.* 2016). All TEC perturbation observations are derived from 30 s data from the SOPAC (http://sopac.ucsd.edu/) Hawaii GPS array in the case of Haida Gwaii and Kuril, and from Pacific Ocean island stations forming part of the Japanese GEONET GPS network in the case of Tohoku. Tsunami amplitude data were recorded by DART buoys and detided according to Watada *et al.* (2014). A summarize of the GPS TEC and DART data reconstructed in this section is provided in Table 3.

In all cases, the normal modes were computed with atmospheric models evaluated at the time and location of the tsunami's arrival and with the ocean depth of the observation area.

The perturbations associated with each tsunami were computed using two types of source: a single-point source located at the epicentre and an extended source corresponding to several point sources distributed along the fault plane. The source parameters used in the point source simulations were those of the CMT project (Dziewonski *et al.* 1981), while those for the extended sources were the finite fault source models from the U.S. Geophysical Survey (http://earthquake.usgs.gov/) for the three events (Hayes 2011). The extended source seismograms were then computed by summing seismograms from all subfaults, each being represented by a point source.

Fig. 13 compares the models computed with a single-point source and an extended source to observed data in TEC perturbation and in tsunami height in the case of the 2012 Haida Gwaii event. As expected, a single-point source generates too high a TEC perturbation amplitude and tsunami displacement. The amplitude of the first wave is reduced for the extended source model due to the interferences between all the point sources. Both the modeled TEC perturbation and modeled tsunami fit the DART and TEC data well for the amplitude of the first wave. The validity of our method was then confirmed by the very good fit obtained in the case of Kuril (Fig. 14) and Tohoku (Fig. 15). Note that as point source models overestimate the amplitudes, only the results from the extended source model were shown and compared with observed data in these last two figures.

However, even if we can reproduce fairly well the main wave in TEC and in tsunami height, the normal modes modeling shows

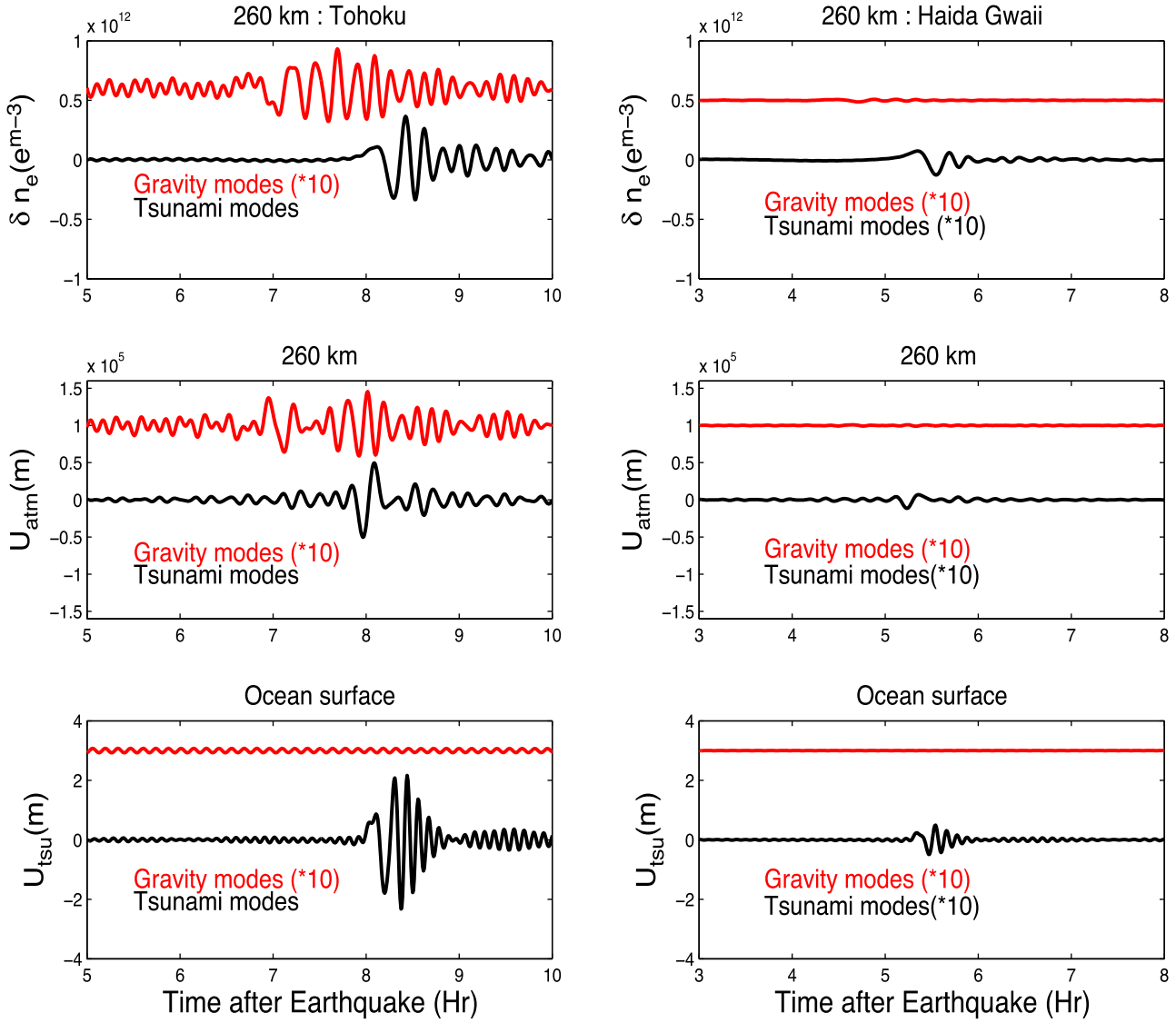


**Figure 12.** From top to bottom: perturbed electron density at 260 km ($\delta n_e$), displacement projected on the magnetic field at 260 km ($U_{\text{atm}}$) and vertical displacement at the ocean surface ($U_{\text{tsu}}$). The Tohoku case study is shown on the left and Haida Gwaii on the right.

**Table 2.** Peak of the electron density perturbation generated by the fundamental gravity modes and the tsunami modes in the case of the Tohoku and Haida Gwaii events.

| $\delta n_e$ ($e^- m^{-3}$) | Tohoku | Haida Gwaii | Threshold detection |
|---|---|---|---|
| Tsunami modes | $3.6 \times 10^{11}$ | $7.33 \times 10^9$ | $\approx 5 \times 10^9$ |
| Fundamental gravity modes | $3.31 \times 10^{10}$ | $8.5 \times 10^8$ | |

**Table 3.** Summarize of data used for comparison with normal mode modeling for the Haida Gwaii, Kuril and Tohoku event.

| | Haida Gwaii | Kuril | Tohoku |
|---|---|---|---|
| GPS ground station | kosm | radf | 1098 |
| GPS satellite | 07 | 17 and 29 | 09 and 12 |
| Dart station | 51 407 | 51 407 | 52 401 |
| Filtering frequency range (mHz) | 0.2–2.6 | 1.0–2.6 | 1.0–2.0 |

some limitations. Indeed, as our 1D normal mode model does not take into account the variation in ocean depth, we have to apply a time-shift to fit the arrival time of the waves to observations. It corresponds to −9.5 min in the case of Haida Gwaii, −11.7 min in the case of Kuril and −15.2 min in the case of Tohoku.

In addition, a second wave, arriving about 20 min after the first one, is not modeled. It is inverted in amplitude and most likely corresponds to the coastal reflection near the source, which cannot be reproduced by the simple 1-D global Earth model used.

In summary, the results obtained are promising but limited by the 1-D approach. If this approach is partially mitigated by the computation of normal modes with the bathymetry corresponding to the observation location, the 3-D effects on the waveform are not modeled and only the first wave amplitude can therefore be modeled. Future steps will have to focus on the impact of the ocean depth variation and the coastal reflection effects on the waveform. This will likely be computational challenging for 3-D tsunami modes as the large bathymetry variations cannot be handle by perturbation techniques.

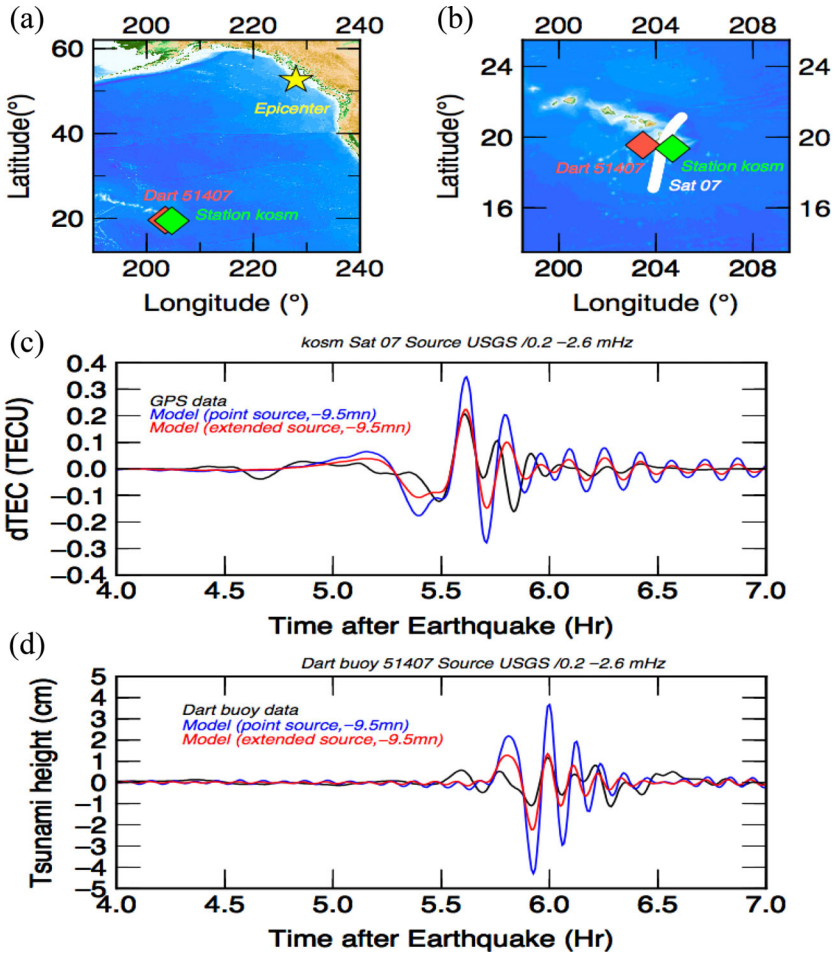


**Figure 13.** 2012 Haida Gwaii tsunami situation map and forward modeling results. (a) Map centred on the location of the 2012 Haida Gwaii tsunami. (b) Map centred on Hawaii. The white line marks the plot of the KOSM station (satellite 07 sounding path) from 4 to 7 hr after the earthquake. (c) Perturbed TEC for the KOSM station (satellite 07 path). (d) Tsunami amplitude recorded by DART buoy 51407. We filtered observed data (black curve) and modeled data (blue and red curves for the point source and extended source case, respectively) between 0.2 and 2.6 mHz. Both point source and extended source models are shown. A time-shift of −9.5 min is applied to the model.

## 9 CONCLUSIONS

Tsunami normal modes can be computed for 1-D Earth models integrating not only the solid Earth but also the atmosphere, and can be used to model the tsunami-induced sea level DART or ionospheric TEC signals, as well as any other seismic or geodetic signals recorded by the tsunami-induced deformations of the solid Earth.

We have illustrated this forward modeling by computation of the tsunami normal modes in Hawaii using the local ocean depth and the atmospheric structure at the time of the tsunami's arrival. We have shown that resonance between tsunami normal modes and the atmosphere occurs at 1.5, 2 and 2.5 mHz. Indeed, at these frequencies, the tsunami branch crosses the atmospheric gravity branches and there is major coupling between the ocean and the atmosphere. Conversely, there is resonance in the oceanic gravity waves at these frequencies. Energy is transferred from the atmosphere to the water. As the group velocity of the fundamental atmospheric gravity modes is slightly faster than that of the tsunami, an atmospheric gravity wave should arrive before the tsunami signal. This is confirmed by seismograms modeling both the sea level height and atmospheric winds, and might be an interesting line of research in order to clarify ionospheric tsunami precursor signals such as those observed by Makela *et al.* (2011).

Our results first demonstrate that accurate modeling of ionospheric tsunami signals requires the integration of atmospheric compressibility, which significantly changes the wavelength and propagation properties of tsunami waves in the atmosphere. At 1.5 mHz, the vertical wavelength is relatively small and the wave can oscillate several times in the atmospheric gravity waveguide before reaching an altitude of about 285 km, where it transits to an evanescent wave. Below this altitude, the phase shift between the real and imaginary part of the wave is indeed $\pi/2$ which is characteristic of a propagative regime. Above 2 mHz, the vertical wavelength is longer than at 1.5 mHz and the height of the gravity waveguide decreases. The wave oscillates only once before becoming evanescent. These effects increase even further for larger frequencies, and for the 2.5 mHz resonance, the vertical wavelength is so long (300 km) that the wave is fully damped well before reaching the thermosphere. Its amplitude is mostly damped by the gravity cut-off and it is not very sensitive to attenuation processes, with an imaginary part 200 times smaller than the real one. At the altitude of the $F_2$ peak (around 300 km), the resonant modes at 2 and 2.5 mHz therefore have very small amplitudes. This explains why reported TEC observations show large spectral amplitudes at 1.5 mHz, but not at 2 or 2.5 mHz.

We then investigated sensitivity to bathymetric properties. The modes were computed for 12:00 LT in Hawaii for an ocean depth of

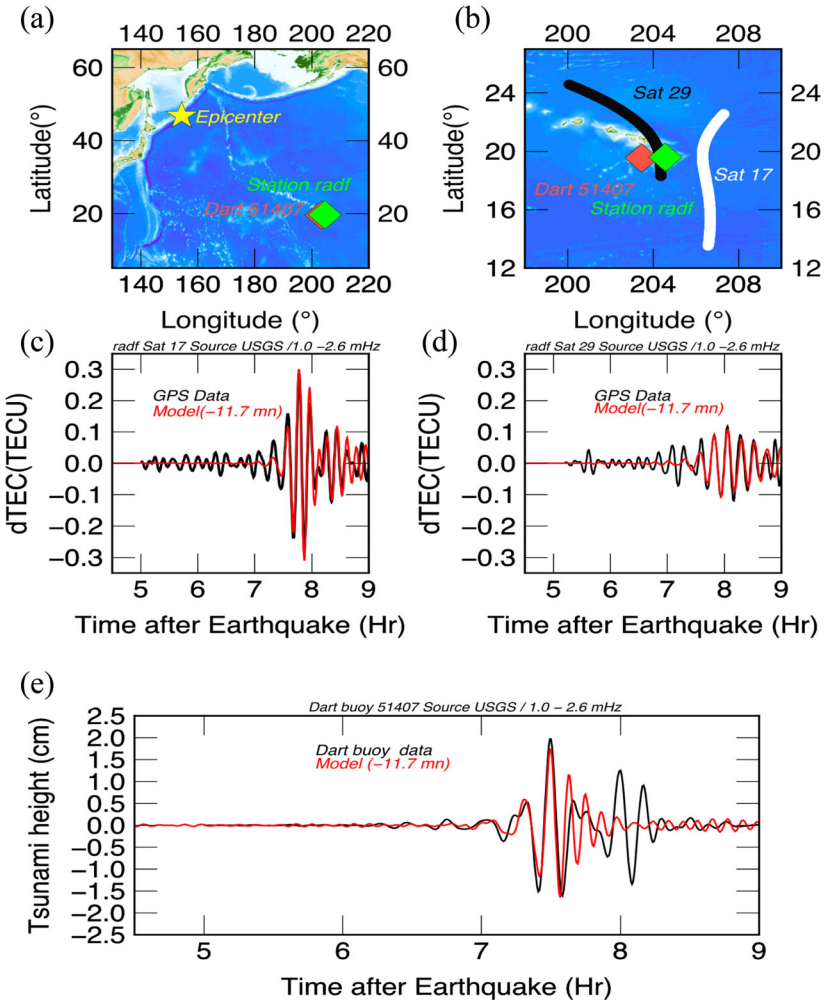


**Figure 14.** 2006 Kuril Islands tsunami situation map and forward modeling results. See Fig. 13 for a description of the panels. We filtered observed data and modeled data between 1 and 2.6 mHz. A time-shift of −11.7 min is applied to the model.

4, 5 and 6 km. As the phase velocity of the tsunami modes strongly depends on ocean depth, the frequencies at which resonances occur also depend on bathymetric properties. The modes for a 6 km depth are highly resonant. There is a major impact on the eigenfunction of normal modes at resonances between 1.3 and 1.7 mHz only at low altitudes (up to 70 km). At higher altitudes, the mode is attenuated by atmospheric viscosity. We also performed a sensitivity study to local time, which revealed that the effect of local time is larger at low frequencies with a clear daytime and night-time regime at the 1.5 mHz resonant frequency. Such a large impact on the amplitude of normal modes must be taken into account in all modeling, and climatic atmospheric models such as NRLMSIS-00 are essential.

We concluded by comparing several DART and TEC observations with the results of modeling for three moderate to large tsunamis generated by the 2012 Haida Gwaii, the 2006 Kuril Islands and the 2011 Tohoku earthquakes. The agreement between observed and synthetics data using an extended source model was good for both the tsunami height (compared to DART) and the perturbed TEC (which are compared to GNSS-TEC (Global Navigation Satellite System) for the first arrival. The arrival time of the first tsunami wave is however affected by variations in ocean depth along the tsunami propagation path and a time-shift must therefore be applied to the modeling results in order to correct these lateral variation effects. A secondary tsunami wave, most likely related to coastal reflection, is not modeled through the 1-D method, where the ocean waveguide is global. These promising results suggest that tsunami normal modes summation is a promising technique for modeling and inverting GNSS-TEC data in order to estimate the variation in tsunami water height from the measured ionospheric data. This will be investigated in a future paper.

## ACKNOWLEDGEMENTS

This work has been fully supported by the US Office of Naval Research through the TWIST project (ONR grant N000141310035 and ONR Global grant N62909-13-1-N270). We would like to thank M. Drilleau, E. Astafyeva, P. Coisson, G. Occhipinti, Y. Nishikawa and F. Karakostas for fruitful discussions as well as two anonymous reviewers for their constructive reviews. We acknowledge the GNSS data provider: the Geospatial Information Authority of Japan (GSI), the Pacific GPS Facility of University of Hawaii, the USGS Hawaiian Volcano Observatory and the Global GNSS Network (GGN), which is operated by UNAVCO at the direction of the Jet Propulsion Laboratory (JPL) for the National Aeronautics and Space Administration (NASA) with support from NASA under NSF Cooperative Agreement No. EAR-1261833 as well as the operator of the DART networks. The data for this paper are available by contacting the corresponding author at rakoto@ipgp.fr.

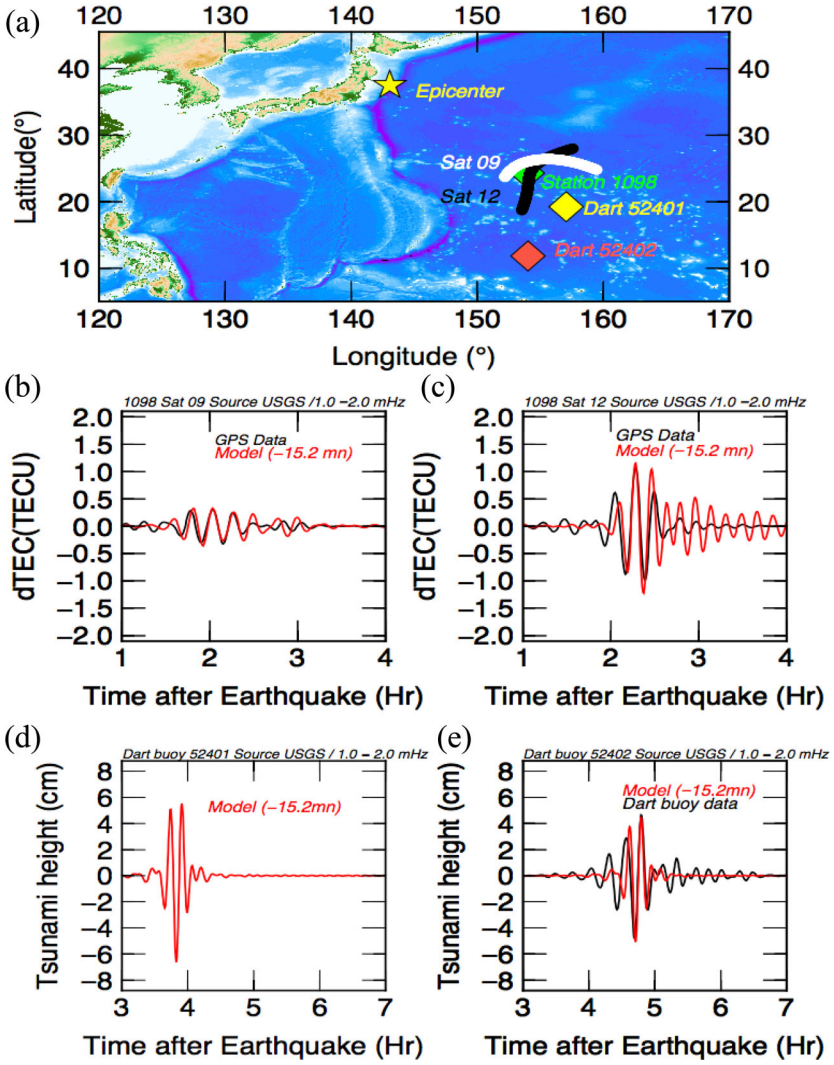


**Figure 15.** 2011 Tohoku tsunami situation map and forward modeling results. See Fig. 13 for a description of the panels. We filtered observed and modeled data between 1 and 2 mHz. A time-shift of −15.2 min is applied to the model. The DART 52401 was not operational at the time of the tsunami and only the modeled tsunami is therefore shown in contrary to the right bottom panel, where both the data and modeled tsunami are shown for the DART 52402.

## REFERENCES


Artru, J., Lognonné, P. & Blanc, E., 2001. Normal modes modeling of post-seismic ionospheric oscillations, *Geophys. Res. Lett.,* **28**(4), 697–700.

Artru, J., Farges, T. & Lognonné, P., 2004. Acoustic waves generated from seismic surface waves: propagation properties determined from Doppler sounding observations and normal-mode modeling, *Geophys. J. Int.,* **158**(3), 1067–1077.

Artru, J., Ducic, V., Kanamori, H., Lognonné, P. & Murakami, M., 2005. Ionospheric detection of gravity waves induced by tsunamis, *J. geophys. Res,* **160,** 840–848.

Boudin, F. *et al.*, 2013. Analysis and modeling of tsunami-induced tilt for the 2007, m = 7.6, Tocopilla and the 2010, m = 8.8 Maule earthquakes, Chile, from long-base tiltmeter and broadband seismometer records, *Geophys. J. Int.,* **194,** 269–288.

Coïsson, P., 2012. Détection multi-instruments des perturbations ionosphériques générées par la propagation des tsunamis, *PhD thesis,* Institut de Physique du Globe de Paris.

Coïsson, P., Occhipinti, G., Lognonné, P., Molinié, J.P. & Rolland, L.M., 2011. Tsunami signature in the ionosphere: a simulation of OTH radar observations, *Radio Sci.,* **46,** RS0D20, doi:10.1029/2010RS004603.

Coïsson, P., Lognonné, P., Walwer, D. & Rolland, L.M., 2015. First tsunami gravity wave detection in ionospheric radio occultation data, *Earth Space Sci.,* **2**(5), 125–133.

Comer, R.P., 1984. Tsunami generation: a comparison of traditional and normal mode approaches, *Geophys. J. Int.,* **77**(1), 29–41.

Dahlen, F.A. & Tromp, J., 1999. *Theoretical Global Seismology,* Vol. 80, 79 pp., Princeton Univ. Press.

Dziewonski, A.M. & Anderson, D.L., 1981. Preliminary reference Earth model, *Phys. Earth planet. Inter.,* **25**(4), 297–356.

Dziewonski, A.M., Chou, T.-A. & Woodhouse, J.H., 1981. Determination of earthquake source parameters from waveform data for studies of global and regional seismicity, *J. geophys. Res.,* **86,** 2825–2852.

Francis, S.H., 1973. Acoustic-gravity modes and large scale traveling ionospheric disturbances of a realistic, dissipative atmosphere, *J. geophys. Res.,* **78,** 2278–2301.

Francis, S.H., 1975. Global propagation of atmospheric gravity waves: a review, *J. Atmos. Terr. Phys.,* **37,** 1001–1054.

Galvan, D.A., Komjathy, A., Hickey, M.P. & Mannucci, A.J., 2011. The 2009 Samoa and 2010 Chile tsunamis as observed in the ionosphere using GPS total electron content, *J. geophys. Res.,* **116,** A06318, doi:10.1029/2010JA016204.

Garcia, R.F., Bruinsma, S., Lognonné, P., Doornbos, E. & Cachoux, F., 2013. GOCE: the first seismometer in orbit around the Earth, *Geophys. Res. Lett.,* **40**(5), 1015–1020.

Garcia, R.F., Doornbos, E., Bruinsma, S. & Hébert, H., 2014. Atmospheric gravity waves due to the Tohoku-Oki tsunami observed in the thermosphere by GOCE, *J. geophys. Res.,* **119,** 4498–4506.

Gilbert, A.M. & Dziewonski, F., 1975. An application of normal mode theory to the retrieval of structural parameters and source mechanisms from seismic spectra, *Phil. Trans. R. Soc. A: Math. Phys. Eng. Sci.,* **278**(1280), 187–269.

Godin, O.A., 2006. Anomalous transparency of water-air interface for low-frequency sound, *Phys. Rev. Lett.,* **97,** 164301, doi:10.1103/PhysRevLett.97.164301.

Godin, O.A., Zabotin, N.A. & Bullett, T.W., 2015. Acoustic-gravity waves in the atmosphere generated by infragravity waves in the ocean, *Earth Planets Space,* **67**(1), 47, doi:10.1186/s40623-015-0212-4.

Grawe, M.A. & Makela, J.J., 2015. The ionospheric responses to the 2011 Tohoku, 2012 Haida Gwaii, and 2010 Chile tsunamis: effects of tsunami orientation and observation geometry, *Earth Space Sci.,* **2**(11), 472–483.

Hayes, G.P., 2011. Rapid source characterization of the 2011 mw 9.0 off the pacific coast of Tohoku earthquake, *Earth Planets Space,* **63**(7), 4, doi:10.5047/eps.2011.05.012.

Hickey, M.P., Schubert, G. & Walterscheid, R.L., 2009. Propagation of tsunami-driven gravity waves into the thermosphere and ionosphere, *J. geophys. Res.,* **114,** A08304, doi:10.1029/2009JA014105.

Hickey, M.P., Schubert, G. & Walterscheid, R.L., 2010. Atmospheric airglow fluctuations due to a tsunami-driven gravity wave disturbance, *J. geophys. Res.,* **115,** A06308, doi:10.1029/2009JA014977.

Hines, C., 1972. Gravity waves in the atmosphere, *Nature,* **239**(5367), 73–78.

Kamogawa, M. *et al.*, 2016. A possible space-based tsunami early warning system using observations of the tsunami ionospheric hole, *Sci. Rep.,* **6,** 37989, doi:10.1038/srep37989.

Kanamori, H. & Mori, J., 1992. Harmonic excitation of mantle Rayleigh waves by the 1991 eruption of Mount Pinatubo, Philippines, *Geophys. Res. Lett.,* **19**(7), 721–724.

Kherani, E.A. *et al.*, 2012. Modeling of the total electronic content and magnetic field anomalies generated by the 2011 Tohoku-Oki tsunami and associated acoustic-gravity waves, *Geophys. J. Int.,* **191**(3), 1049–1066.

Kherani, E.A., Rolland, L., Lognonné, P., Sladen, A., Klausner, V. & de Paula, E.R., 2016. Traveling ionospheric disturbances propagating ahead of the Tohoku-Oki tsunami: a case study, *Geophys. J. Int.,* **204**(2), 1148–1158.

Kobayashi, N., 2007. A new method to calculate normal modes, *Geophys. J. Int.,* **168**(1), 315–331.

Komjathy, A. *et al.*, 2012. Detecting ionospheric TEC perturbations caused by natural hazards using a global network of GPS receivers: the Tohoku case study, *Earth Planets Space,* **64**(12), 1287–1294.

Landau, L.D. & Lifshitz, E.M., 1958. *Course of Theoretical Physics,* Vol. 7, pp. 326–327, doi:10.1016/0891-3919(58)90200-6.

Lognonné, P., 1991. Normal modes and seismograms in an anelastic rotating Earth, *J. geophys. Res.,* **96,** 20 309–20 319.

Lognonné, P., Clévédé, E. & Kanamori, H., 1998. Computation of seismograms and atmospheric oscillations by normal-mode summation for a spherical earth model with realistic atmosphere, *Geophys. J. Int.,* **135**(2), 388–406.

Lognonné, P. *et al.*, 2006. Ground-based GPS imaging of ionospheric post-seismic signal, *Planet. Space Sci.,* **54**(5), 528–540.

Mai, C.-L. & Kiang, J.-F., 2009. Modeling of ionospheric perturbation by 2004 Sumatra tsunami, *Radio Sci.,* **44,** RS3011, doi:10.1029/2008RS004060.

Makela, J.J. *et al.*, 2011. Imaging and modeling the ionospheric airglow response over Hawaii to the tsunami generated by the Tohoku earthquake of 11 March 2011, *Geophys. Res. Lett.,* **38,** L00G02, doi:10.1029/2011GL047860.

Massel, S., 2015. *Internal Gravity Waves in the Shallow Seas,* Springer.

Melgar, D. & Bock, Y., 2015. Kinematic earthquake source inversion and tsunami runup prediction with regional geophysical data, *J. geophys. Res.,* **120**(5), 3324–3349.

Meng, X., Komjathy, A., Verkhoglyadova, O.P., Yang, Y.-M., Deng, Y. & Mannucci, A.J., 2015. A new physics-based modeling approach for tsunami-ionosphere coupling, *Geophys. Res. Lett.,* **42**(12), 4736–4744.

Millot-Langet, R., Clévédé, E. & Lognonné, P., 2003. Normal modes and long period seismograms in a 3D anelastic elliptical rotating Earth, *Geophys. Res. Lett.,* **30**(5), 1202–1206.

Nishida, K., 2000. Resonant oscillations between the solid Earth and the atmosphere, *Science,* **287**(5461), 2244–2246.

Occhipinti, G., Lognonné, P., Kherani, E.A. & Hébert, H., 2006. Three-dimensional waveform modeling of ionospheric signature induced by the 2004 Sumatra tsunami, *Geophys. Res. Lett.,* **33,** L20104, doi:10.1029/2006GL026865.

Occhipinti, G., Kherani, A.E. & Lognonné, P., 2008. Geomagnetic dependence of ionospheric disturbances induced by tsunamigenic internal gravity waves, *Geophys. J. Int.,* **173**(3), 753–765.

Occhipinti, G., Dorey, P., Farges, T. & Lognonné, P., 2010. Nostradamus: the radar that wanted to be a seismometer, *Geophys. Res. Lett.,* **37,** L18104, doi:10.1029/2010GL044009.

Occhipinti, G., Coïsson, P., Makela, J.J., Allgeyer, S., Kherani, A., Hébert, H. & Lognonné, P., 2011. Three-dimensional numerical modeling of tsunami-related internal gravity waves in the Hawaiian atmosphere, *Earth Planets Space,* **63**(7), 847–851.

Occhipinti, G., Rolland, L., Lognonné, P. & Watada, S., 2013. From Sumatra 2004 to Tohoku-Oki 2011: the systematic GPS detection of the ionospheric signature induced by tsunamigenic earthquakes, *J. geophys. Res.,* **118**(6), 3626–3636.

Okal, E.A., 1982. Mode-wave equivalence and other asymptotic problems in tsunami theory, *Phys. Earth planet. Inter.,* **30**(1), 1–11.

Okal, E.A., 1988. Seismic parameters controlling far-field tsunami amplitudes: a review, *Nat. Hazards,* **1**(1), 67–96.

Park, J. & Gilbert, F., 1986. Coupled free oscillations of an aspherical, dissipative, rotating earth: Galerkin theory, *J. geophys. Res.,* **91**(B7), 7241–7260.

Peltier, W.R. & Hines, C.O., 1976. On the possible detection of tsunami by a monitoring of the ionosphere, *J. geophys. Res.,* **81**(12), 1995–2000.

Picone, J.M., Hedin, A.E., Drob, D.P. & Aikin, A.C., 2002. NRLMSISE-00 empirical model of the atmosphere: statistical comparisons and scientific issues, *J. geophys. Res.,* **107,** 1468, doi:10.1029/2002JA009430.

Rolland, L.M., Occhipinti, G., Lognonné, P. & Loevenbruck, A., 2010. Ionospheric gravity waves detected offshore Hawaii after tsunamis, *Geophys. Res. Lett.,* **37,** L17101, doi:10.1029/2010GL044479.

Rolland, L.M., Lognonné, P. & Munekane, H., 2011a. Detection and modeling of Rayleigh wave induced patterns in the ionosphere, *J. geophys. Res.,* **116,** A05320, doi:10.1029/2010JA016060.

Rolland, L.M., Lognonné, P., Astafyeva, E., Kherani, E.A., Kobayashi, N., Mann, M. & Munekane, H., 2011b. The resonant response of the ionosphere imaged after the 2011 off the Pacific coast of Tohoku Earthquake, *Earth Planets Space,* **63,** 853–857.

Satake, K., 2002. 28 Tsunamis, in *International Geophysics,* Vol. 81, pp. 437–451, Elsevier.

Titov, V., Rabinovich, A.B., Mofjeld, H.O., Thomson, R.E. & González, F.I., 2005. The global reach of the 26 December 2004 Sumatra tsunami, *Science,* **309,** 2045–2048.

Tsai, V.C., Ampuero, J.P., Kanamori, H. & Stevenson, D.J., 2013. Estimating the effect of Earth elasticity and variable water density on tsunami speeds, *Geophys. Res. Lett.,* **40**(3), 492–496.

Vadas, S.L., Makela, J.J., Nicolls, M.J. & Milliff, R.F., 2015. Excitation of gravity waves by ocean surface wave packets: upward propagation and reconstruction of the thermospheric gravity wave field, *J. geophys. Res.,* **120**(11), 1–33.

Watada, S., 2009. Radiation of acoustic and gravity waves and propagation of boundary waves in the stratified fluid from a time-varying bottom boundary, *J. Fluid Mech.,* **627,** 361–377.

Watada, S., 2013. Tsunami speed variations in density-stratified compressible global oceans, *Geophys. Res. Lett.,* **40**(15), 4001–4006.

Watada, S. *et al.*, 2006. Atmospheric pressure change associated with the 2003 Tokachi-Oki earthquake, *Geophys. Res. Lett.,* **33,** L24306, doi:10.1029/2006GL027967.

Watada, S. & Kanamori, H., 2010. Acoustic resonant oscillations between the atmosphere and the solid Earth during the 1991 Mt. Pinatubo eruption, *J. geophys. Res.,* **115,** B12319, doi:10.1029/2010JB007747.

Watada, S., Kusumoto, S. & Satake, K., 2014. Traveltime delay and initial phase reversal of distant tsunamis coupled with the self-gravitating elastic Earth, *J. geophys. Res.,* **119**(5), 4287–4310.

Widmer, R. & Zürn, W., 1992. Bichromatic excitation of long-period Rayleigh and air waves by the Mount Pinatubo and El Chichon volcanic eruptions, *Geophys. Res. Lett.,* **19**(8), 765–768.

Woodhouse, J.H., 1974. Methods in Computational Physics, Volumes 11 and 12, Volume 11–Seismology: Surface Waves and Earth Oscillations, Volume 12–Seismology: Body Waves and Sources, B. A. Bolt (Editor), (Academic Press, New York; London), *Geophys. J. Int.,* **39**(1), 201–202.

Woodhouse, F.A. & Dahlen, J.H., 1978. The effect of a general aspherical perturbation on the free oscillations of the earth, *Geophys. J. Int.,* **53**(2), 335–354.

Yu, Y., Yan, Z. & Hickey, M.P., 2015. Lower thermospheric response to atmospheric gravity waves induced by the 2011 Tohoku tsunami, *J. geophys. Res.,* **120**(6), 5062–5075.

Yuan, X., Kind, R. & Pedersen, H.A., 2005. Seismic monitoring of the Indian Ocean tsunami, *Geophys. Res. Lett.,* **32,** L15308, doi:10.1029/2005GL023464.

## APPENDIX: HORIZONTAL AND VERTICAL DISPLACEMENT QUADRATURE PHASE SHIFT

The $\pi/2$ phase shift between the vertical and horizontal displacements just above the ocean surface can be easily explained theoretically. Indeed, in the plane wave approximation and Cowling approximation (i.e. when mass redistribution is neglected), where $\mathbf{U} = \mathbf{U}_0 \exp(i(\omega t - kx))$, projection to the $x$-axis of eqs (1) and (2) leads to:

$$-\rho\omega^2 V = ik(p_{\text{Hooke}} + \rho g U), \tag{A1}$$

$$p_{\text{Hooke}} = -\rho c_{\text{sound}}^2 \left( \frac{\partial U}{\partial r} - ikV \right), \tag{A2}$$

where $U$ and $V$ are, respectively, the vertical and horizontal components of the T normal modes displacement in the ocean and $p_{\text{Hooke}}$ is the pressure change associated with fluid compressibility. Similar expressions can be obtained in the case of a sphere. These two equations lead to:

$$\frac{V}{U} = -ik\frac{g - \frac{c_{\text{sound}}^2}{U}\frac{\partial U}{\partial r}}{\omega^2 - k^2 c_{\text{sound}}^2} = -\frac{i}{k}\frac{g - \frac{c_{\text{sound}}^2}{U}\frac{\partial U}{\partial r}}{c_{\text{tsunami}}^2 - c_{\text{sound}}^2}. \tag{A3}$$

In the ocean, vertical displacement increases almost proportionally from the bottom of the ocean to the surface and $\frac{\partial U}{\partial r} = U_0/D$, where $U_0$ is the vertical amplitude of the ocean surface and $D$ the depth of the ocean. This leads to the following amplitude ratio at the surface, where $V_0$ is the horizontal amplitude of the ocean surface:

$$\frac{V_0}{U_0} = -\frac{i}{kD}. \tag{A4}$$

This explains the quadrature phase shift between the vertical and horizontal components of water displacement at the surface of the ocean as well as the much larger horizontal amplitudes as $kD \ll 1$.